229 (2023) 212101

Contents lists available at ScienceDirect

Geoenergy Science and Engineering

journal homepage: www.sciencedirect.com/journal/geoenergy-science-and-engineering

Coupled multiphase flow, geochemical, and geomechanical modelling of the impact of shale interlayers on CO_2 migration

Ali Alsayah [a,b], Sean P. Rigby [a,b,*]

[a] Department of Chemical and Environmental Engineering, Faculty of Engineering, University of Nottingham, University Park, Nottingham, NG7 2RD, UK
[b] Geo-energy Research Centre, University of Nottingham, University Park, Nottingham, NG7 2RD, UK

ARTICLE INFO

Keywords:
Shale inter-layer
Porosity
Diffusion
Capillary breakthrough pressure
Mineral dissolution
Deformation

ABSTRACT

The need to find sufficient capacity for geological carbon dioxide (CO_2) storage to meet demand means less-than ideal, heterogeneous reservoirs need to be considered. Many such reservoirs are apparently compartmentalised by inter-layers, which may help, or hinder, CO_2 migration and storage capacity, depending upon their nature. The impact of shale inter-layers of thicknesses below seismic resolution are generally neglected in plume migration simulations, but have been shown here to be important. Only simulations of plume migration that include coupling of all three of mass transport, geo-chemical and geo-mechanical processes together provide proper prediction of the barrier efficiency of relatively thin shale inter-layers. A series of feedback inter-actions between these three process types has been studied in detail, and, for example, leads to the unexpectedly higher barrier efficiency of thin inter-layers compared to slightly thicker inter-layers. The results show that capillary breakthrough pressure, diffusion processes and re-activation of natural fractures played a vital role in enhancing the migration of the CO_2 plume via the thicker shale inter-layers towards the overburden. This paper identifies significant research gaps regarding the effects of complicated, intricate processes affecting shale inter-layer (or seal) integrity under realistic reservoir conditions.

1. Introduction

One option in order to reduce overall greenhouse gas emissions, to mitigate anthropogenic global warming, is to capture carbon dioxide (CO_2) at source and store (sequester) it in a suitable reservoir (IPCC, 2005). This procedure is known as carbon capture and storage (Global CCS Institute, 2020). To make a significant contribution to reduction of emissions, a large number of suitable reservoirs are required. For example, Noy et al. (2012) estimated that a modern gas-fired power station of 1 GW net electrical capacity with 90% capture would require a store with capacity of around 2.5 Mt CO_2 per annum. Hence, a large number of suitable stores with large capacity are required. However, the numbers of ideal reservoirs, such as uniform sandstone aquifers roofed entirely with a single, continuous impermeable seal, are too rare to satisfy demand.

Therefore, it has been necessary to explore the storage capability of less-than ideal stores, such as those with reservoir rocks containing internal barriers, such as deformation bands and shale interlayers, and incomplete seals, such as those with baffle-like arrangements. The internal architecture of a reservoir can significantly impact on plume migration, and, thus, potential storage capacity. For example, Pourmalek et al. (2021) studied the impact of small-scale deformation bands in Penrith Sandstone to assess how far these features can create effective mini-traps and, thereby, contribute to secure CO_2 geological storage. These workers suggested that the relevant literature exhibited conflicting findings concerning the permeability contrast, between deformation bands and reservoir rock, needed for the former to act as barriers to flow in the latter. Deformation bands can act as either flow conduits or barriers, with the latter due to cementation. Pourmalek et al. (2021) conducted simulations of CO_2 injection into sandstones with random or deterministic distributions of deformation bands, with variable band clustering density, band geometry, orientation and permeability. The presence of conjugated (crossing) bands could improve storage security, but increased tilting away from the horizontal, along the line of intersection, led to increasing spillage. More vertically-orientated, parallel bands accentuated upward overall flow towards the seal. However, this study only considered flow phenomena, and did not consider coupled geochemical and geomechanical processes affecting the deformation

* Corresponding author. Department of Chemical and Environmental Engineering, Faculty of Engineering, University of Nottingham, University Park, Nottingham, NG7 2RD, UK.
E-mail address: sean.rigby@nottingham.ac.uk (S.P. Rigby).

https://doi.org/10.1016/j.geoen.2023.212101
Received 23 November 2022; Received in revised form 28 June 2023; Accepted 2 July 2023
Available online 6 July 2023

bands.

In some ways, the Sleipner reservoir in the North Sea might also be considered a non-ideal reservoir, and is currently a test site for CCS. Sleipner was the World's first commercial storage project, and CO_2 injection started in 1996. The injection rate is typically 0.9 Mt pa (MIT, 2022). Bitrus et al. (2016) report that the reservoir rock of the Sleipner field, namely the Utsira Sand, as a seismically resolvable unit with a sharp top and base, which is interbedded with over ten intra-reservoir mudstone or shale layers. Each shale interlayer has an average thickness of ~1.3 m as interpreted from gamma ray and neutron density logs.

The understanding of the geometry of the shale inter-layers within a reservoir is of importance for injection planning and migration prediction, as subtle differences between barrier horizons can have a decisive influence on flow pathways and reservoir efficiency, in terms of ongoing storage capacity (Zweigel et al., 2000). Greater tortuosity in the plume migration path leads to greater reservoir volumes being swept out and greater storage capacity (Green and Ennis-King, 2009). Further, the uncertainty surrounding the sealing efficiency of an unreliable caprock may be offset if internal reservoir heterogeneities sufficiently delay flow from reaching the caprock itself over the long-term. While a few studies have been performed including both fully coupled chemical-mechanical effects, together with two-phase flow modelling, of CO_2 injection into a relatively uniform geological formation, only minor attention has been given to the impact of impermeable inter-layers on directing plume migration during, and post, CO_2 injection, and, then, only focusing on the caprock sealing performance. The simulation of fully-coupled flow, geochemical and geomechanical processes during carbon sequestration has recently been reviewed (Rigby et al., 2022). For example, Ojala (2011) and Fleury et al. (2011) have investigated the impact of chemical-mechanical coupled processes on the caprock sealing performance and the outcomes have shown that after thousands of years of exposure, only the lowest few metres of the caprock may be affected by the CO_2-rich fluid, and also, the effects on mechanical properties were minor. Green and Ennis-King (2009) have studied the impact of random spatial distributions of shale inter-layers within a reservoir on plume migration, but geomechanical-geochemical coupling was neglected. Agartan et al. (2017) studied CO_2 injection into a sandstone reservoir with multiple, continuous shale inter-layers of varying thickness (1–10 m) and permeability. While the study showed shale inter-layers disrupted convective mixing and enhanced lateral spreading of CO_2, it only considered mass transport (diffusion and flow) effects, along with dissolution, and neglected coupled geomechanical effects. Elenius and Gasda (2013) found that horizontal, tight shale layers reduce dissolution rates, especially for long barriers, in contrast to the results for random heterogeneity in permeability that enhanced dissolution (Farajzadeh et al., 2011). CO_2 can penetrate thin clay layers by diffusion and can, thereby, facilitate plume persistence beyond the clay layer (Park et al., 2021). Zhou and Burbey (2016) considered hydromechanical effects within a complementary model where disconnected sand bars of various geometries were distributed within a mudrock seal, but did not include geochemical effects. Hence, no studies include the full trio of coupled geomechanical, geochemical and flow behaviour for reservoirs with inter-layers, and, thus, properly study the impacts of such inter-layers on plume migration.

This study proposes a numerical model that is used to test a set of simulation scenarios wherein the full trio of mechanical-chemical-hydrological processes are coupled, given this complete set of interactions is typically omitted in previous work. It will be shown that, for complex reservoirs with higher degrees of heterogeneity, this more comprehensive coupling of processes is needed to understand, and predict, the idiosyncratic direction taken by the evolution of the plume behaviour in the different scenarios.

The generalised structural models developed here are used to analyse the potential for the development of localized leakage pathways via shale inter-layers with different thicknesses, in a reservoir that has some similarities to the Utsira Sand of the Sleipner reservoir, but is (merely Sleipner-like and) not intended as a direct representation of this reservoir. This is because the impact of temporal evolution of shale interlayers is typically neglected in previous work on many reservoirs. The field-scale reactive transport model was built using hydrogeological, geochemical, and geomechanical information from the Sleipner gas field, which is located within the North Sea, about 250 km west of Stavanger, Norway, as merely a typical example of such data. We also consider the interaction between shale inter-layers and a basement when both are present. Additionally, the model will include, the mechanical impacts of the buoyancy force, $scCO_2$ dissolution in the brine (Shukla et al., 2010), variation in spatial distribution of porosity, and permeability across the reservoir and the shale inter-layers due to lithological variation during sedimentary deposition, and variability of rock characteristics and mineralogy because of chemical processes. Furthermore, specific focus will be on interactions between changes in in-situ stresses and geo-mechanical characteristics, due to $scCO_2$ injection, and, also, mineral precipitation and dissolution due to CO_2-rock interaction. Further, investigations were made of how particular geological features, such as the seal natural fracture re-activation during the injection, affected plume migration. All the above-mentioned objectives will be investigated by setting six different case studies. Overall, the study will consider if compartmentalisation of the reservoir with thin shale inter-layers helps or hinders efficient CO_2 plume distribution and storage.

2. Methodology

Zweigel et al. (2000) reported a distribution of the thickness of shale interlayers within the Utsira Sand based upon gamma ray log data. The thickness distribution ranged from 0.5 to 5 or more metres. In this work thicknesses around those of the tails of this distribution will be selected to consider the range in behaviour that may be possible amongst different layers depending upon thickness. While Zweigel et al. (2000) suggested the shale inter-layers may have faulting, they also suggested they were continuous and of regional extent. It is generally observed that the lateral extent of inter-layers is typically much larger than their vertical separation (Green and Ennis-King, 2009). Hence, laterally extensive, continuous and faulted inter-layers will be considered.

In this work, a three-dimensional Cartesian reservoir model was created with 8000 (40 × 20 x 10) active grids cells and one injection well, which was positioned in the middle of the reservoir with a maximum increase in bottom-hole pressure (BHP) to 18.5 MPa for whole injection period of 100 years, as shown in Appendix 1, Figure A1. As a sensitivity analysis, the simulations for Cases 1 and 2 were also run on grids with 50,000 gridblocks, to check effect of grid size on the findings. The BHP was chosen such that it remains comfortably below the typical fracture pressure for similar reservoirs. A fracture pressure gradient of ~20 MPa/km (IEA, 2010), or 22.5 MPa/km (Pourmalek et al., 2021), is typical. The chosen BHP is similar to, or often less than, that used in previous work, such as 21.4–34 MPa (Pourmalek et al., 2021), 26–34.6 MPa (Mohammed et al., 2012) and 24.5 MPa (Nghiem et al., 2004). The reservoir was closed off by no-flow boundary conditions at the lateral boundaries, to represent a sealing boundary fault condition. This is similar to the compartmentalised reservoir studied by Pourmalek et al. (2021). Zhou and Burbey (2016) have also suggested that, where the research focus is the seal, the no-flow boundary condition allows the pore pressure in the reservoir to reach a relatively high level in a reasonably short simulation time, in order to reduce demand on computing resources. The system domain was initially filled by brine. PVT properties were user defined and calculated at a temperature of 37 ^{O}C, which is the typical reservoir temperature for the Sleipner reservoir. The 3D model was radially symmetric with dimensions of 6 km in the radial direction and 0.22 km in the vertical direction. The reservoir unit was assumed to have a thickness of 220 m and was overlain by a shale inter-layer whose thickness was varied from 0.3 m to 3 m. The top of the simulation domain was taken as 900 m, and the bottom of the simulation

domain as 1120 m, below the ground surface. These depths are deeper than the Sleipner injection location.

Schematic diagrams, of the particular reservoir structures in each Case, are shown in Fig. 1. Case 1 represents a single 3 m shale inter-layer (indicated by the dark brown layer) in a sandstone reservoir (shown by the light brown), whereas Case 2 shows a single 0.3 m shale interlayer (indicated by the dark brown layer) in a sandstone reservoir (shown by the light brown). In contrast, Cases 3 and 4 consist of a system with a combination of 0.3 m and 3 m shale inter-layers but in different vertical order within the sandstone reservoir, and where injection occurs in-between the two interlayers. Each shale interlayer was represented by a single grid block thickness layer in the simulation model, as has been done in previous work in the literature (Sundal et al., 2015). The shale layer was located in layer 5, in the z-direction, for Cases 1, 2, 5, and 6, whereas, for Cases 3 and 4, the shale was located in layers 4 and 9. Cases 5 and 6 represent circumstances similar to those in Cases 1 and 2, respectively, but where the shale inter-layers are also naturally fractured. The modelled region was assumed to be isothermal and the Cartesian-coordinate grid for the fluid-flow modelling divided the reservoir–caprock sequence vertically into ten layers, each consisting of one of two types of rocks, namely sand and shale. In Cases 1, 2, 5, and 6, only layer 5 had low permeability rock (shale), while the rest were high

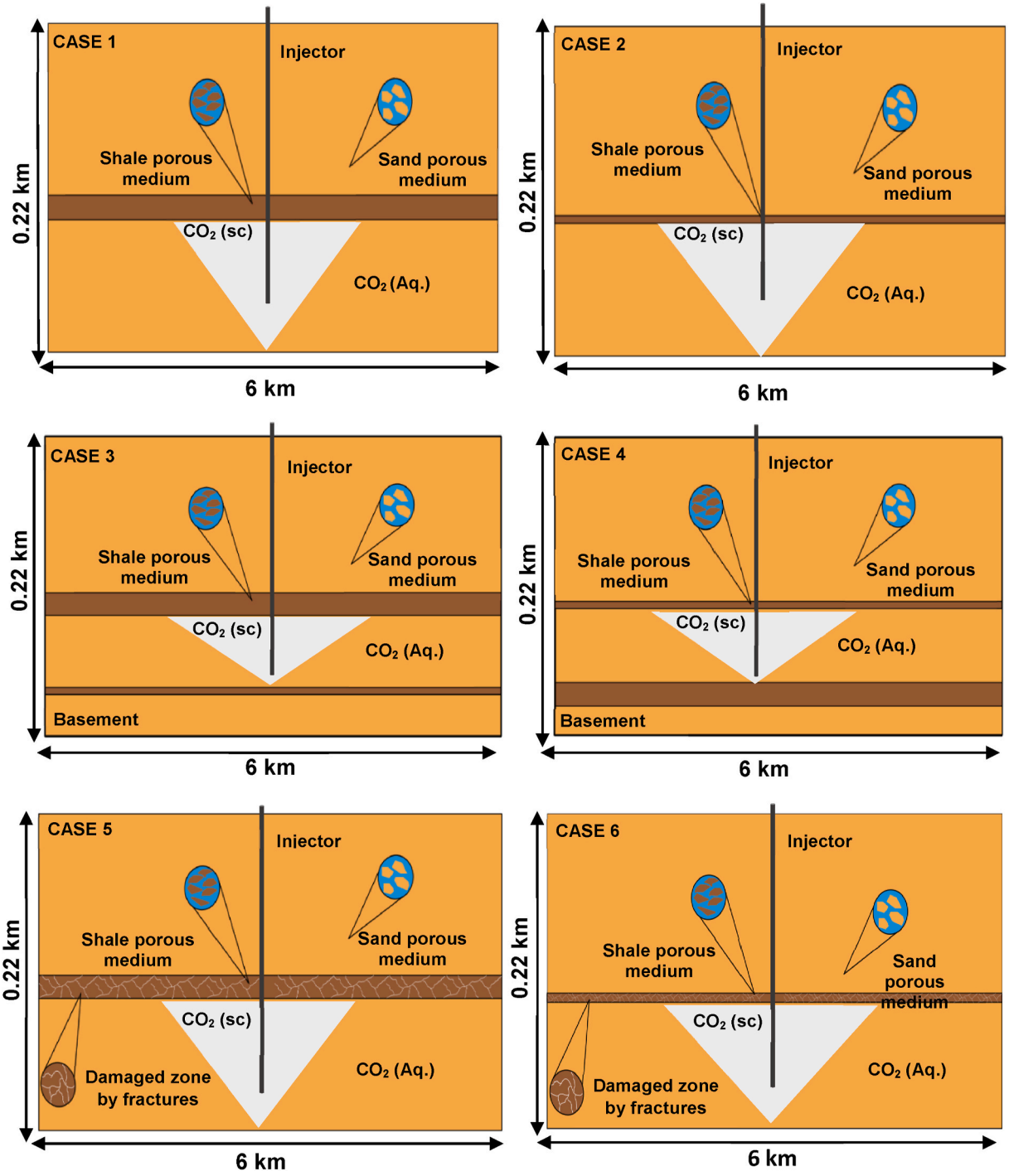

Fig. 1. Schematic diagrams showing the reservoir structures in the Cases that have been used in the study. The white cone indicates the zone of $scCO_2$ injection, and the CO_2 (Aq.) represents the dissolved CO_2 in the resident brine.

permeability rock (sand). Whereas, for Cases 3 and 4, layers 4 and 9 were low permeability rock (shale) and the rest were high permeability rock (sand).

The simulations of $scCO_2$ injection were performed using Computer Modelling Group (CMG) software. The overall methodology for coupling flow, geomechanics and geochemical processes implemented in the CMG software is that described by Tran et al. (2009). The Builder software was used to populate the simulation model parameters and the numerical settings. The well-established, multiphase, compositional flow software, GEM, was used to carry out the injection simulations (CMG-GEM, 2020). GEM can efficiently perform dual permeability calculations by including fluid flow between matrix and fractures. In addition, it provides the capability of modelling the reservoir's post-injection responses. The water and gas relative permeability curves were obtained using the Brooks-Corey equation, and the capillary pressure curve was computed by the Van Genuchten approach which takes into account zero capillary pressure for full brine saturation (Zhang et al., 2016). The focus of this study was on the nature of the rising CO_2 front, which is wholly a drainage displacement, and, also, the imbibition process occurring after the end of injection. Therefore, gas relative permeability hysteresis and water-gas capillary pressure hysteresis have been used. The CMG-Winprop software was used to determine fluid properties of the reservoir, and the supercritical CO_2 density was calculated with the Peng-Robinson Equation of State (1978). Also, the gas viscosity was estimated from the Jossi, Stiel and Thodos correlation. The aqueous phase density and viscosity were calculated from the Rowe and Chou correlation, and the Kestin et al. correlations, respectively. The B-dot model was applied to model the activity coefficient, while Li and Nghiem's method (1986) was applied to model the Henry's law constant, which was used to model the CO_2 solubility in brine. The geomechanical stability was assessed by using the condition of failure as derived from the Mohr column model. The 'confined' boundary conditions used here are those as described in Dean et al. (2003) and Tran et al. (2009), as implemented in the GEM software. The lateral and bottom outside boundaries of the model were permitted zero normal displacement, but the top surface could move freely. The zero-normal displacement boundary condition for the simulation lattice is often used in the literature (for example: Khan et al., 2020a, 2020b; Xiao et al., 2020; Zhou and Burbey, 2016; Gutierrez and Prassetyo, 2017; Haddad and Sepehrnoori, 2017; Varre et al., 2015; Rohmer and Seyedi, 2010) in modelling of CO_2 injection.

Hypothetical fracture zones in the shale inter-layers were constructed in Cases 5 and 6 where the dual-permeability method was used to simulate the shale natural fracture structure, but the Utsira Sand-like reservoir was treated as a single porosity structure. Hence, matrix and fracture collocated blocks were only present in the interlayers. The matrix and fracture collocated blocks have potential fractures in the i-, j- and k-directions. The Gilman and Kazemi (1983) formulation was used for the shape-factor. In addition, the Barton-Bandis model has been utilized to relate the change in the fracture effective stress to the shale fracture permeability (Tran et al., 2009), as will be explained below. As the pressure increases in the regular grid the stresses are altered, causing the stresses on the fractures to increase. Eventually the stress breaks past the failure envelope of the rock, causing a fracture to appear (open) and allow fluids to pass through. If the fracture is mainly caused by tensile stress then the threshold for the fracture normal effective stress will be zero or negative, whereas, if failure is mainly caused by shear stress parallel to the fracture direction, then the failure criterion may be positive since the failure may obey Mohr-Coulomb criteria (Tran et al., 2009). In this work, fractures suffered shear failure. The Barton-Bandis model calculates the permeability of a fracture as a function of the fracture normal effective stress $\sigma_n^{'}$. In the undrained condition, the stress is partly carried by the solid framework and partly by the fluid, and so the normal effective stress, for a given component, is calculated using the following expression:

$$\sigma_n^{'} = \sigma - \alpha p \tag{1}$$

where α is Biot's coefficient and p stands for pore pressure. The normal effective stress for a fracture is illustrated in a schematic diagram in the Appendix (see Figure A2). The particular fracture direction that fails is determined by the values of the various loads applied to the block.

The mean effective stress, $\sigma_m^{'}$, is the average of the normal effective stresses, given by:

$$\sigma_m^{'} = \frac{1}{3}\left(\sigma_{11}^{'} + \sigma_{22}^{'} + \sigma_{33}^{'}\right) \tag{2}$$

For values of the fracture normal effective stress larger than the opening fracture stress f_{rs}, the permeability remains low. If $\sigma_n^{'}$ falls below the threshold value of f_{rs}, then the permeability increases instantaneously to its maximum value khf, and will remain there until the $\sigma_n^{'}$ increases again. At a point, the permeability is reduced instantly to the fracture closure permeability, $kccf$, and, as the $\sigma_n^{'}$ increases further, the permeability tends asymptotically to the residual value of fracture closure $krcf$, as will be seen below. Thus, fracture permeability depends not only on the normal effective stress, which is equivalent to minimum principle effective stress, but also on its history.

The fracture permeability k_f is calculated from:

$$k_f = kccf\left(\frac{e}{e_0}\right)^4 \geq krcf \tag{3}$$

where $kccf$ is the fracture closure permeability (mD), and e is the fracture aperture, given by:

$$e = e_0 - V_j \tag{4}$$

and e_0 is the initial fracture aperture (a length), and V_j is the joint closure at normal fracture effective stress $\sigma_n^{'}$ as given by:

$$V_j = \frac{\sigma_n^{'}}{kni + \sigma_n^{'}/V_m} \tag{5}$$

where V_m is the maximum fracture closure (a length) given by:

$$V_m = e_0\left[1 - \left(\frac{krcf}{kccf}\right)^{\frac{1}{4}}\right] \tag{6}$$

where $krcf$ is the residual value of the fracture closure permeability (mD). The Barton-Bandis model was only applied to shale inter-layers to represent the natural fractures within the inter-layers for Cases 5 and 6.

In this study, for all Cases 1–6, the coupling of fluid flow and geomechanics, with geochemical reactions, was achieved using an iteratively two-way coupled approach (Dean et al., 2003) as follows. The fluid flow module in CMG-GEM computed the amount of CO_2 dissolution and flow in the formation, the geochemical reactions, any changes in pressure, temperature, and compositions, and also any changes in porosity and permeability due to said geochemical reactions (Tran et al., 2005, 2009). The computed pressure and temperature are then passed onto the geomechanics module, which calculated stress changes, and any deformation in the formation and nearby layers. The solution from the geomechanics module was then sent back again to the fluid simulator via coupling variables including porosity and permeability (Tran et al., 2009). These two variables are then used to obtain new values of pressure and temperature which are re-sent to the geomechanics module, where they are re-computed. This iterative process continues in a given time step until the convergence criterion was satisfied (the tight level in the GEM software). Examples of the cumulative material balance error for the simulations described below are shown in the Appendix (Figure A3). The error was significantly smaller (by orders of magnitude) than any changes to rock porosity and the particular observed effects described below. The geochemical modelling assumed that pore volume changes resulted not only by volumetric deformation but, also,

because of geochemical interactions. The considerations of thermal processes were as follows. The initial formation temperature in the model was assumed to change with depth. The reservoir temperature directly affected the kinetics of the chemical reactions, and the CMG-GEM simulator could also account for the thermal changes during CO_2 injection. However, an isothermal condition was assumed for all Cases 1–6, and it was assumed that the CO_2 reaches each layer of the formation at the corresponding formation temperature.

The CO_2 injection rate was constant through the injection period (100 years), and in all scenarios, and it was set to 40,000 m^3/day at surface conditions (pressure 1 atm, temperature 15 °C) as shown in Appendix 1, Figure A4. This is equivalent to 0.03 Mt/y. This rate was chosen based upon what the Utsira sand reservoir can withstand according to a study by Gasda et al. (2017) which concluded that Utsira sandstone can hold over 100 Mt/y of CO_2. Then, the well was shut down, and thereafter the sealing integrity was monitored over both the short-term (200 years) and long-term (10,000 years).

Due to the inherent heterogeneity of the reservoir formation, geostatistics were used. in the numerical simulation, to characterize that heterogeneity in terms of petrophysical properties, which are summarised in Table 1. The Gaussian method was used to assign random values of porosity and permeability to all 8000 grid blocks to simulate different degrees of heterogeneity for the reservoir and the seal, rather than using a homogenous model. An unconditional, Gaussian, geostatistical simulation method was used to generate multiple versions (called realizations) of grid values that all reproduce the statistical data, reproduce the histogram of the data, and reproduce the variogram of the data. This method was used to calculate petrophysical properties, such as porosity and permeability, by setting a uniform distribution type, defined by a minimum and a maximum value, with properties allocated randomly within the model to represent the heterogeneity in the reservoir. This method is useful for testing the influence of heterogeneity when no specific data is available. The resultant grids are shown in Appendix Figure A5 . The vertical to horizontal permeability ratio (k_v/k_h) was assumed to be 0.5 for Cases 1–4, whereas for Cases 5 and 6 it was assumed to be 0. The reason behind the said setting of this latter ratio is because the initial value of the ratio will not have an effect since reactivation of fractures will take place and the vertical permeability will then increase, and also the setting of a very low fracture permeability, to effectively represent a zero-flow boundary, was to show the re-activation process. Key parameters of the models are included in Tables 1–6. The stress values given in Table 4 are interpreted as effective stresses and are used by the geomechanics module to initialize the value of stress in the geomechanics set of equations. This can then evolve during the course of the simulations.

The reference capillary pressure, and gas, and water relative permeability, curves which have been used in the simulation are shown in Appendix 1, Figure A6. The capillary pressure curve was for Nordland shale rock, starting with capillary pressure of 0 kPa and endpoint of 10,000 kPa at irreducible water. The entry pressure had an inverse relationship with the pore radius of a typical pore throat, whereas absolute permeability varied with the square of the pore throat radius. The reference capillary pressure, and gas and water relative permeability curves, which have been used in the simulation are given in Appendix 1, Figure A7. The curve is for Utsira Sandstone formation rock with capillary pressure of 0 kPa and endpoint of 30 kPa at irreducible water.

Table 1
Hydrological parameters, used for the model, from Sleipner field for Cases 1–6 (Springer and Lindgren, 2006; Lothe A and Zweigel, 1999; Holloway et al., 2000; Yang and Aplin, 2004; Lindeberg et al., 2000; Audigane et al., 2006; Amann et al., 2011).

	Utsira Sand	Nordland shale
Vertical Permeability, mD	550–2500	0.000375–0.00075
Horizontal Permeability, mD	1100–5000	0.00075–0.0015
Porosity, %	27–40%	17–36%
Initial reservoir pressure, kPa	9000	
Initial pressure gradient, MPa/km	10	
Rock compressibility, 1/kPa	4.5×10^{-13}	
Diffusion Coefficient (cm^2/s)	4×10^{-8}	

Table 2
Fracture properties used for Cases 5 and 6 (Cavanagh and Haszeldine, 2014).

Property	Value
Natural Fracture porosity, %	10
Natural Fracture permeability, mD	0.00075–0.0015
Fracture opening permeability, mD	35
Fracture closure permeability, mD	5
Initial fracture stiffness, kPa/m	6.78×10^7
Natural fracture aperture, m	2×10^{-6}
Fracture opening stress, kPa	3200
Natural fracture spacing, m	10

Table 3
Mechanical properties used for Cases 1–6 which were taken from data for Sleipner field (Park et al., 2021).

Utsira Sand		Nordland Shale	
Young's modulus, kPa	6.3e5	Young's modulus, kPa	3e5
Poisson's ratio	0.3	Poisson's ratio	0.25
Friction angle/°	19.1	Friction angle/°	20.4
Cohesion, kPa	450	Cohesion, kPa	800
Shear stress, kpa	3000	Shear stress, kPa	2650

Table 4
In-situ stresses for the lithologies applied to Cases 1–6 (Park et al., 2021).

σ_x	σ_y	σ_z	σ_{xy}	σ_{yz}	σ_{xz}
4660 kPa	4660 kPa	7770 kPa	0	0	0

Table 5
Initial composition of the formation water, taken from Sleipner field and applied for Cases 1–6 (Audigane et al., 2006).

Parameters	Value	Elements	Concentration
Temperature, °C	37	Al	1.3e-8
pH	7.67	Ca	7.4e-3
Salinity of brine, (PPM)	32,000	Fe	1.0e-8
		K	5.3e-4
		Na	4.5e-1
		SiO_2	1.6e-4

Table 6
Mineralogical compositions of the Utsira Sand and Nordland Shale from Sleipner field which have been used for Cases 1–6 (Audigane et al., 2006).

Utsira Sand composition	Volume fraction	Nordland Shale composition	Volume fraction
Albite-low	0.030	Albite-low	0.132
Calcite	0.067	Calcite	0.010
Chalcedony	0.769	Chalcedony	0.334
Muscovite	0.052	Muscovite	0.251
Kaolinite	0.001	Kaolinite	0.195
K-feldspar	0.069	K-feldspar	0.023
Siderite	0.011	Siderite	0.001

3. Results

3.1. Cases 1-4

3.1.1. Flow

Fig. 2 shows the plume position following 100 years of injection of $scCO_2$ for Cases 1 and 2. Fig. 2(a)–(c) show an x-z plane cross-sectional

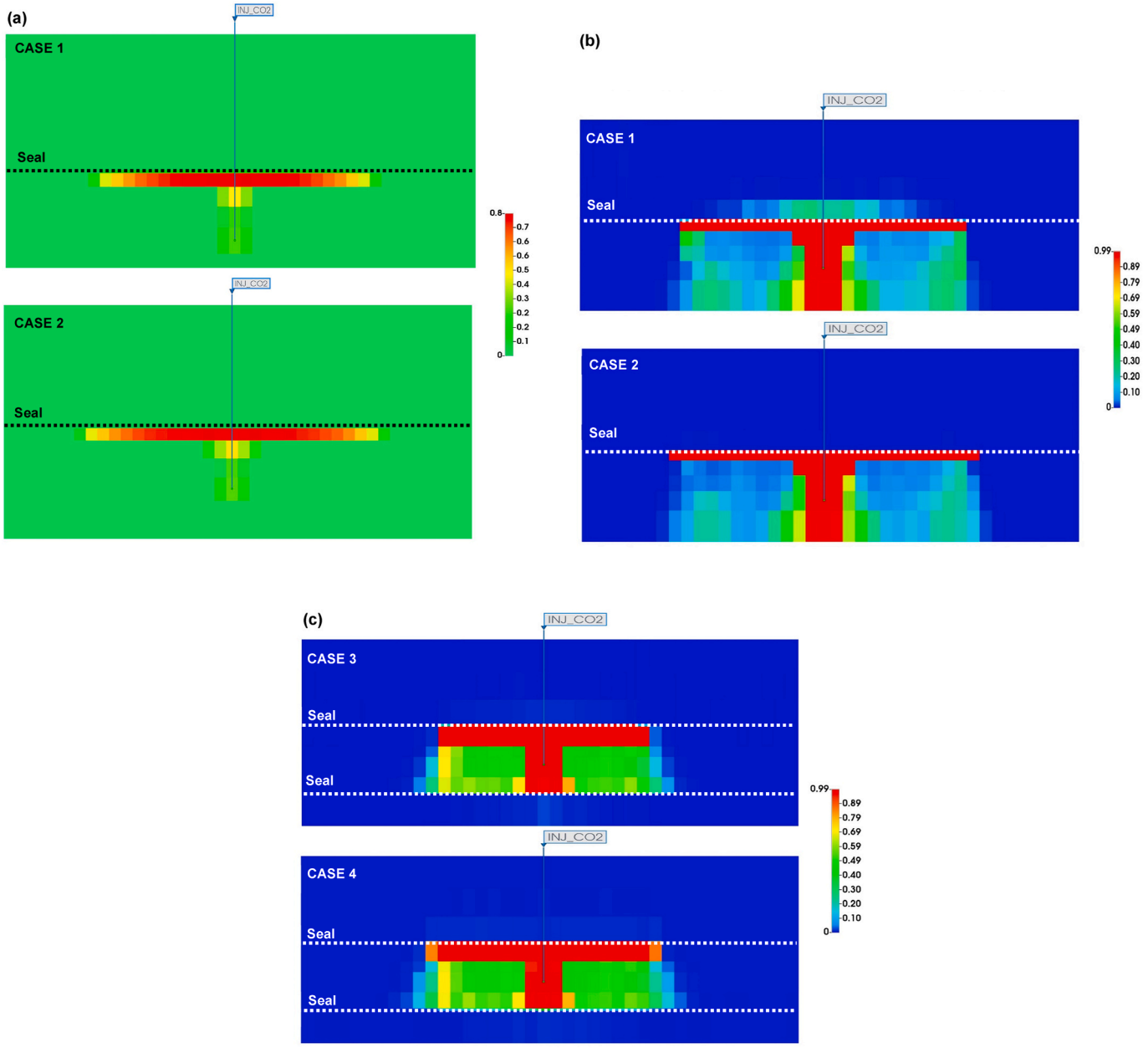

Fig. 2. CO_2 plume migration behaviour after 100 years of injection for (a and b) Cases 1 and 2, and (c) Cases 3 and 4. The colour bar in (a) indicates the gas saturation fraction of $scCO_2$ only, and (b and c) bar shows the global mole fraction of 'CO_2' (mole fraction of 'CO_2' in aqueous phase + mole fraction of 'CO_2' in sc phase).

view, with a cut-off in the y-direction at J = 10, of the simulated models. The black or white dashed lines indicate the position of the shale inter-layer locations in the models to more clearly define where the profiles of the $scCO_2$ plumes have penetrated into the shale, but not leaked into the overburden in both Cases, as seen in Fig. 2 (a). This upwards migration was controlled by both absolute permeability and capillary entry pressure, where the main process behind upwards migration is buoyancy-driven migration. From a comparison of the plume behaviour for the two seal thicknesses, of 3 m (Case 1) and 0.3 m (Case 2), respectively, in Fig. 2(b), it can be seen that the CO_2 in the aqueous phase (Shukla et al., 2010) plume managed to escape the 3 m shale inter-layer after 100 years of injection, but the 0.3 m layer managed to hold back the plume from leaking into the sandstone above. Further, Fig. 2(c) shows a comparison, between Cases 3 and 4, of CO_2 plume migration for systems with multiple shale inter-layers. From Fig. 2(c), it can be seen that both Case 3 and Case 4 have not shown any major leakage via either shale inter-layer.

The much greater leakage of CO_2 through the thicker shale inter-layer in Case 1, compared to the thinner inter-layer in Case 2, is counter-intuitive. The following description of wide-ranging findings, concerning the concomitant geomechanical and geochemical effects, is to provide the background necessary to then explain this unexpected finding for mass transport behaviour of the inter-layers.

3.1.2. *Geomechanics*

Fig. 3 shows comparison plots, for Cases 1 and 2 during the first 200 years of simulated time, of the pore pressure change for (a) within the shale inter-layers, where the specific observation point was located at co-ordinates (17, 10, 5), in x-y-z directions, respectively, and also (b) within the sandstone just under the shale inter-layers, where the observation point was located at co-ordinates (17, 10, 6). For the injection to start, the injection pressure needs to be higher than the pore

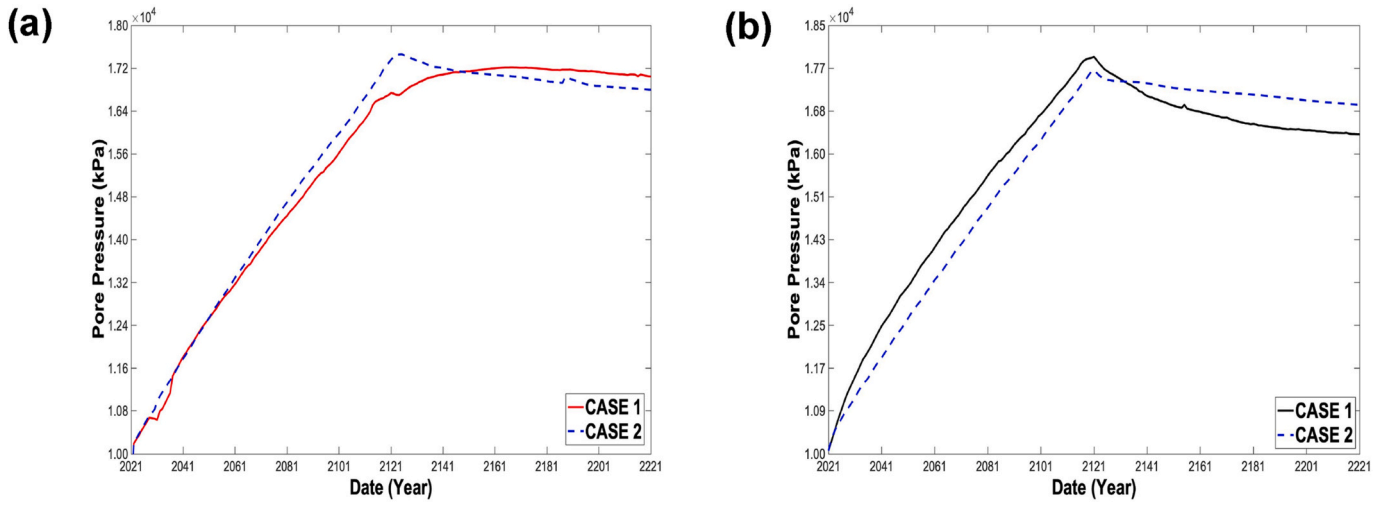

Fig. 3. The variation in pore pressure with time within each shale inter-layer (a) and the sandstone directly under the shale inter-layers (b) for Cases 1 and 2.

entry pressure which was set to be 9 MPa for the reservoir initial pressure. Due to the difference in capillary pressure, the pore pressure upon injection builds to 9.3 MPa (a) and 10 MPa (b) for Cases 1 and 2.

Fig. 4 shows a comparison plot of the pore pressure change within the lower and upper shale inter-layers during the 200 years of simulated time for Cases 3 and 4. The pore-pressure increases during the injection period, but, once the injection well has been shut-in, the increase of pore pressure has dropped. The maximum increase in pore pressure is that for the lower shale layer in Case 3 of 18,398 kPa.

Fig. 5 shows plots of the mean effective stress change over time, for the shale inter-layers in Cases 1–4, that resulted from the pore pressure build-up induced by the injection. These plots show that a significant reduction of effective stress during the early stages of injection was followed by a slight increase during the post-injection period.

Fig. 6 shows the results of a comparison of deformation of the shale inter-layers for Cases 1–4, respectively. During the early stages of injection, there is an increase in the vertical displacement within the shale inter-layers due to an overpressure of the storage formation compared to the seal formation.

A comparison was made of the total normal stress (principal stress) in the vertical and horizontal directions (as seen in Fig. 7) within the shale inter-layers for Cases 1–4. In addition, it can be observed from Fig. 7 that the vertical stress is larger than the horizontal stress at the early stages of injection, which means that plastic strain propagates through the whole thickness of the seal. Whereas, at a later stage of injection, the horizontal stress was larger than the vertical stress which means the plastic strain then propagates horizontally along the contact line with the reservoir. After injection, both stresses showed a minor reduction. It is noted that the model grid blocks that were close to the leakage region had the noticeable difference in the vertical stress between Cases 1 and 2 seen in Fig. 7(a), whereas, for the grid blocks that were far away from the leakage region, the difference in vertical stress was minor between Cases 1 and 2. Hence, the vertical movement of CO_2 via the shale layer in Case 1 caused this difference in the vertical stress compared with Case 2.

Fig. 8 shows the change in the shale inter-layer volume from the initial volume during 200 years of simulation for Cases 1–4. Note: the negative sign represents compression of the layer.

Fig. 9 shows a comparison in terms of the porosity difference between the reservoir porosity and porosity change caused by geomechanics (void difference), for Cases 1, 2, 3, and 4. The calculation of

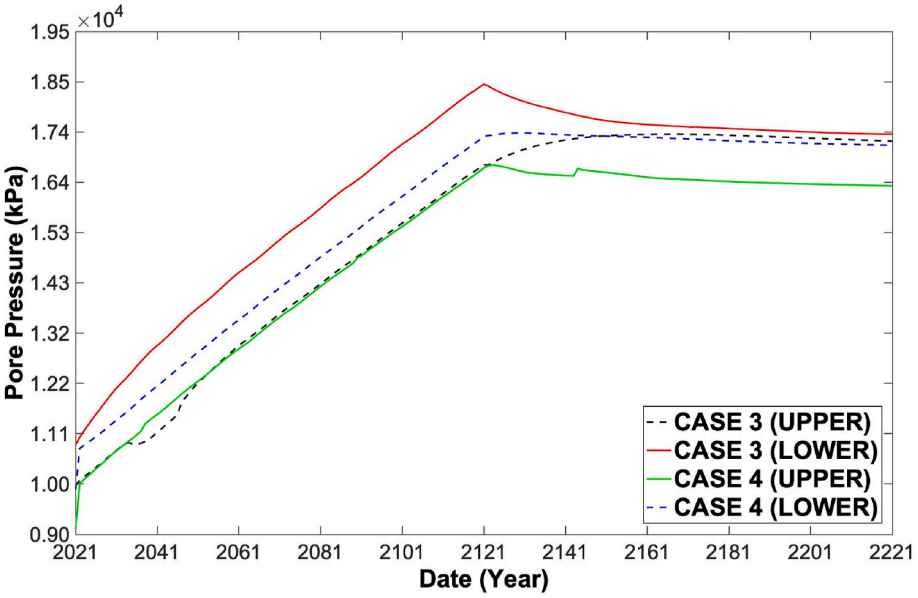

Fig. 4. The variation in pore pressure with time within both the upper and lower shale inter-layers for Cases 3 and 4.

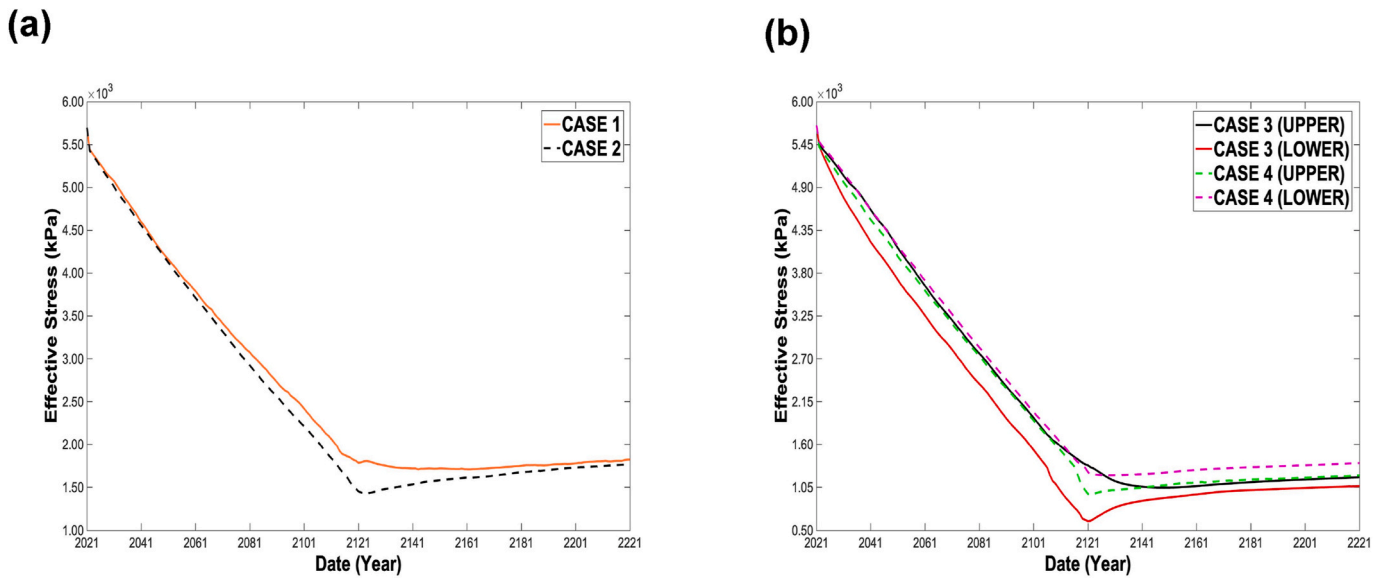

Fig. 5. Temporal change in the mean effective stress of the shale inter-layer for Cases 1 and 2 (a), and of the upper and lower shale inter-layers for Cases 3 and 4 (b).

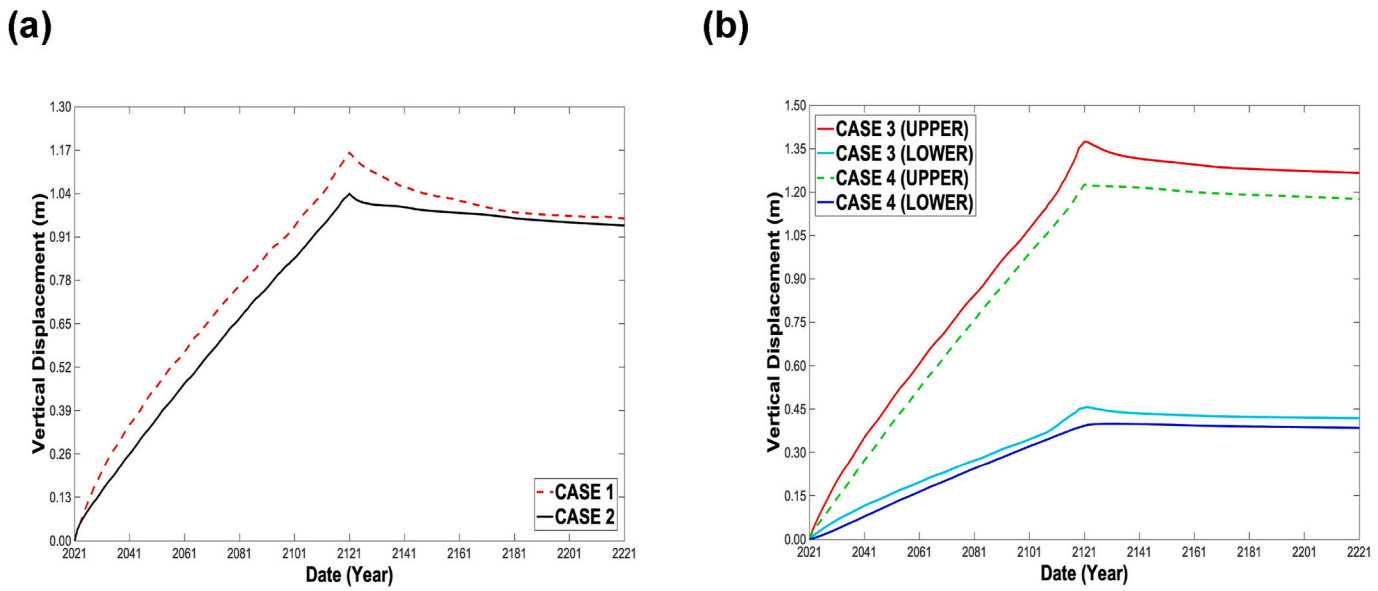

Fig. 6. Vertical displacement change of the shale inter-layer for Cases 1 and 2 (A) and upper, and lower shale inter-layers for Cases 3 and 4 (B) as a function of time.

the said porosity was based upon the pressure and total vertical and horizontal stresses. Further, the porosity change resulted from variation of in-situ stresses due to the pressure build-up introduced by the injection. From the void difference change as a function of time, it can be seen that an increase in the void spaces within the shale inter-layer Case 1 at the early stages of injection was larger compared to that for Case 2. Additionally, Fig. 10 shows the shale inter-layer porosity change caused the overall porosity change due to both geochemistry and geomechanics (A) compared to the porosity change caused by only geomechanics (B) for Cases 1–4.

Fig. 11 shows the porosity change due to different processes, including, combined geochemical and geomechanical (A), and geomechanical alone (B), occurring within the sandstone layers which are directly under the shale inter-layer for Cases 1 and 2.

Fig. 12 shows the porosity changes due to all the various processes, including geomechanical and geochemical, occurring within the shale inter-layers over 10,000 years for Cases 1–4.

Fig. 13 shows that the shale inter-layers had no shear failure over the simulated time for Cases 1 and 2. However, the 0.3 m shale inter-layer in Case 2 was close to shear failure (safety factor has dropped to a value close to zero), especially in the later stage of injection compared to the 3 m shale inter-layer in Case 1. This occurred in Case 2 because the $scCO_2$ kept accumulating in the 0.3 m shale inter-layer and had not leaked into the overburden. On the other hand, some of the $scCO_2$ managed to escape the 3 m shale inter-layer in Case 1. Thus, the 0.3 m shale fluid overpressure was larger than that for 3 m shale inter-layer which caused the initial stress state to be closer to the Mohr-Coulomb failure envelope (the diameter size of Mohr circle increases and the whole circle moved to the left). In other words, the horizontal stress was becoming close to being lower than the vertical stress, which is close to the failure criterion. Additionally, the observation, that can be made from Fig. 13, is that the upper and lower shale inter-layers of Case 3 and 4 reached a failure for limited period (at the end of the injection period). However, no significant shear failure was observed, in either Case, sufficient to cause a serious expansion in the pore volume of the shale inter-layers and cause a leakage.

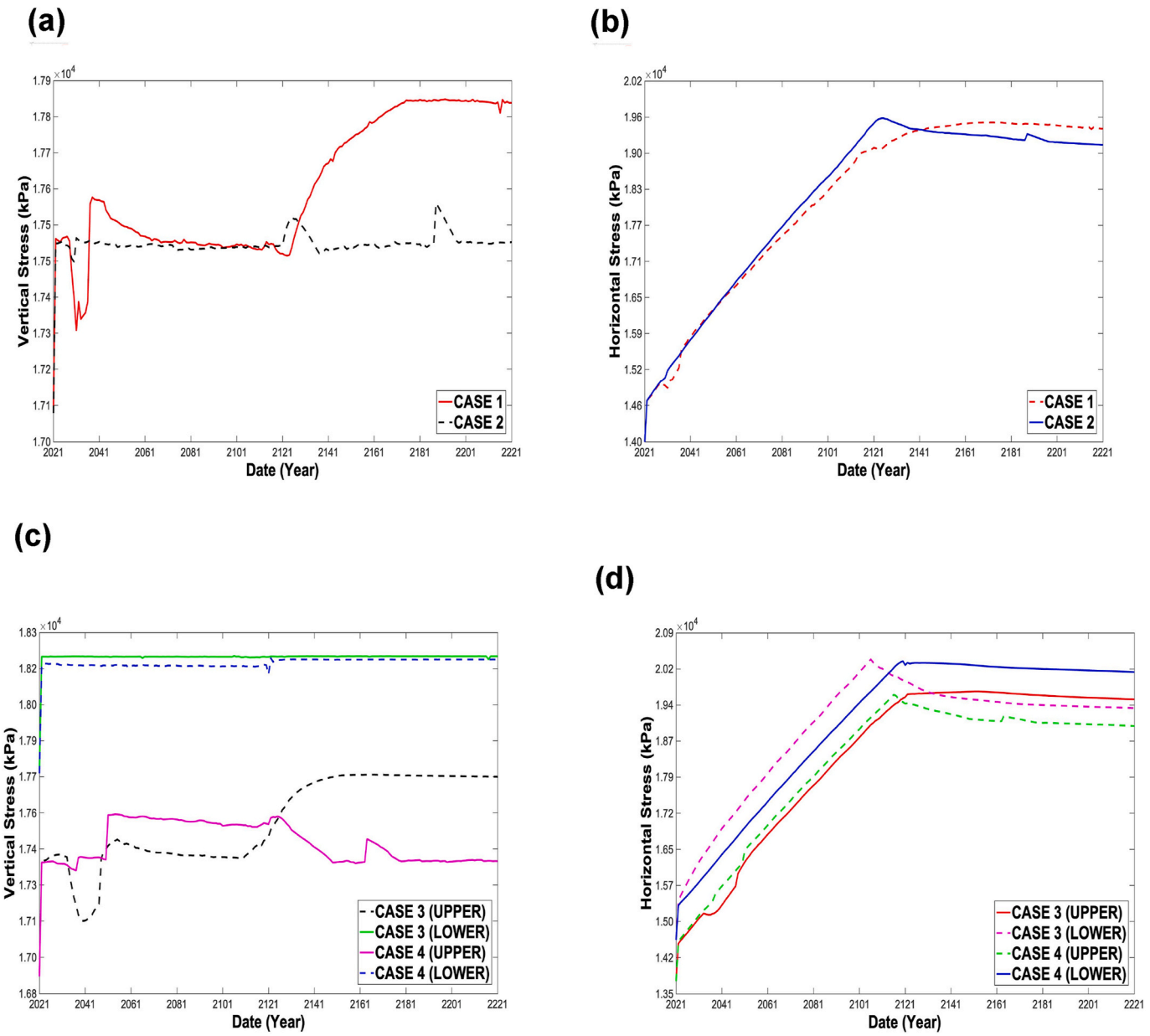

Fig. 7. Variation over time of stress, within the shale inter-layer, in k- (a) and i- (b) directions for Cases 1 and 2, and within the upper and lower shale inter-layers, in k- (c) and i- (d) directions as a function of time for Cases 3 and 4.

Fig. 13 also illustrates a comparison between Cases 1–4 in terms of tensile failure location at the same juncture. Case 1 was far from tensile failure compared to Case 2 which was close to exhibiting a tensile failure located within the shale inter-layer. In addition, the lower shale inter-layer in Case 3 experienced a tensile failure both during, and after, the injection, whereas, the upper shale inter-layer only failed during the injection period. The upper and lower shale inter-layers in Case 4 also encountered failure. However, the failure that occurred in both Cases 3 and 4 was limited to a short period.

Fig. 14 shows a comparison, in terms of the CO_2/brine capillary entry pressure behaviour, of the shale inter-layers as the $scCO_2$ penetrated towards the seal. In addition, Fig. 14 also shows the amount of $scCO_2$ that has managed to invade the shale inter-layer as a function of time for Cases 1–4, where the capillary pressure change based on the gas and water phases saturation.

Fig. 15 illustrates the gas (CO_2) compressibility within the shale inter-layers for Cases 1–4. More gas was compressed in Case 1, compared to Case 2, at the early stages of injection due to the difference in the inter-layer thicknesses. Further, in Cases 3 and 4, the upper seal had the largest gas compressibility, compared to the lower seal, at the early stage of the simulation due to the upwards movement of CO_2 because of the buoyancy force. However, in the later stages, the lower shale inter-layer had more compressed gas compared to the upper shale inter-layer because the fluid density increased as it dissolved into the brine resulting in downwards movement of the high-density saturated plume, towards the lower shale inter-layer, caused by the gravity force.

Fig. 15 also shows the brine compressibility within the shale inter-layers for Cases 1–4, where the water compressibility reduces with time because of the brine compressibility being much lower compared to gas (CO_2) and rock.

Fig. 16 shows a comparison of the total fluids (brine and $scCO_2$) compressibility as a function of time for Cases 1–4. The compressibility depends upon pressure and temperature, and, since the temperature is assumed constant during the simulation, then only pressure will vary with time (isothermal compressibility). As the fluid density changes are directly related to changes in the volume, the interface position will be

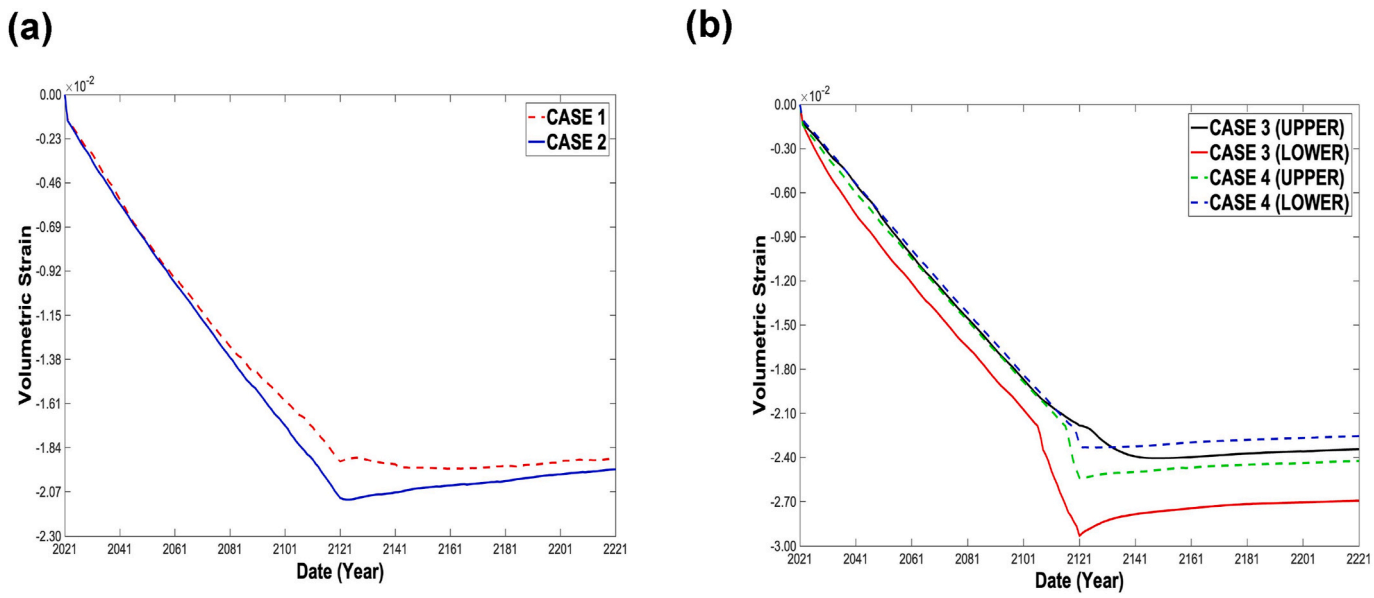

Fig. 8. Volumetric strain behaviour of the shale inter-layer for Cases 1 and 2 (a), and upper, and lower shale inter-layers for Cases 3 and 4 (b), as a function of time.

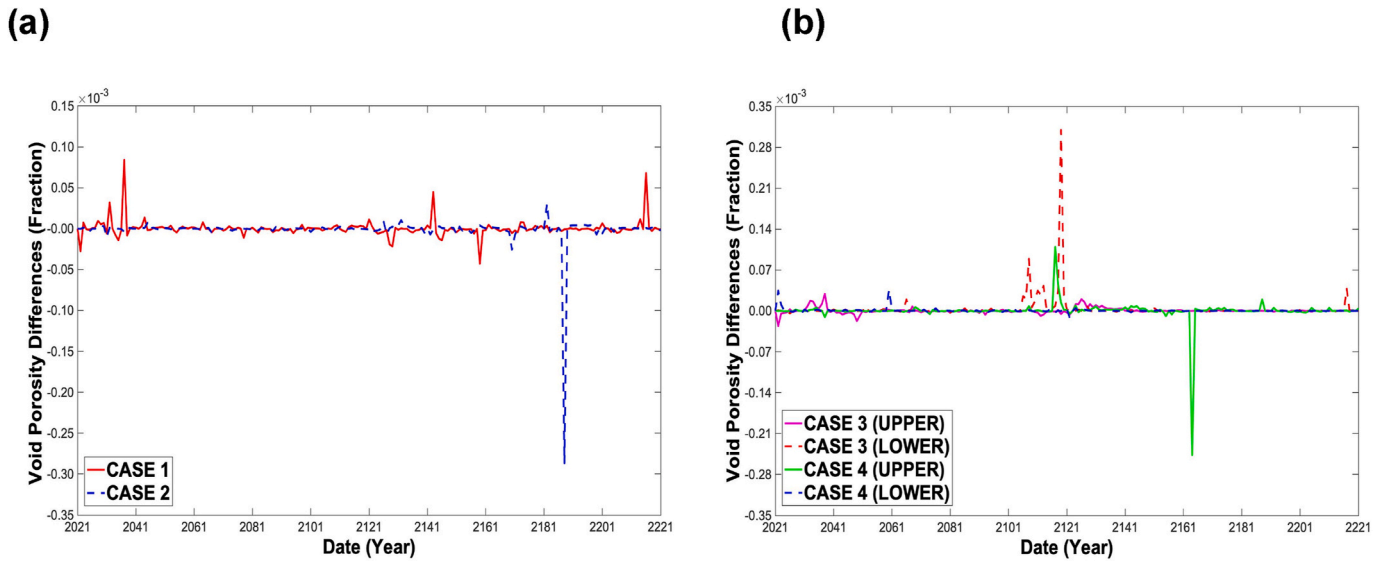

Fig. 9. Void porosity differences (true porosity from geo-mechanical minus reservoir porosity) within the shale inter-layer for Cases 1 and 2 (a) and upper, and lower shale inter-layers for Cases 3 and 4 (b) as a function of time.

affected by compressibility. An increase in compressibility caused a reduction in pressure build-up. The storage capacity mainly depends upon the pore and brine compressibility, which provides extended pore space availability. The injection of CO_2 caused rises in the fluid pressure and displaced the formation of brine laterally. Since the simulated reservoir boundaries are closed, the storage capacity would then be related to rock and fluids compressibility.

3.1.3. *Geochemical processes*

Fig. 17(a&b) show a comparison of the relative importance over time of the different CO_2 sequestration mechanisms in terms of the rate of $scCO_2$ being dissolved into the resident brine, the CO_2 precipitated as minerals, and the CO_2 trapped due to hysteresis, for Cases 1–4. All Cases have shown that, although initial CO_2 injection is in the supercritical phase (sc), with time, CO_2 started to dissolve in the brine, and then this was subsequently followed by mineralization reactions in the aqueous phase, which resulted in a reduction in $scCO_2$ with time and an increase in the amount of dissolved CO_2. Additionally, Case 2 trapped more CO_2 compared to Case 1, and, also, Case 4 had more CO_2 trapped than Case 3 but the difference between them was minor. It can be seen that it takes a very long time for the mineralization reactions to occur, and for CO_2 to be trapped in this form. Further, it can be observed that the amount of CO_2 in minerals is steadily increasing by the end of the simulation.

Fig. 18 shows the precipitation and dissolution of various minerals within the shale inter-layers over 10,000 years for Cases 1–4. It can be seen that the $scCO_2$ penetration into the shale inter-layers induced chemical alteration of the seal, while reactions of calcite, albite-low, muscovite, kaolinite, K-feldspar, and siderite favoured dissolution of the minerals, in contrast, the reactions of chalcedony favoured precipitation.

Fig. 19(a–d) show the brine pH and salinity change in the shale inter-layers as a result of $scCO_2$ injection over time for Cases 1–4. It can be seen that, for all Cases, pH dropped significantly during the first 1000 years, due to the release of hydrogen ions in carbonic acid. Afterwards,

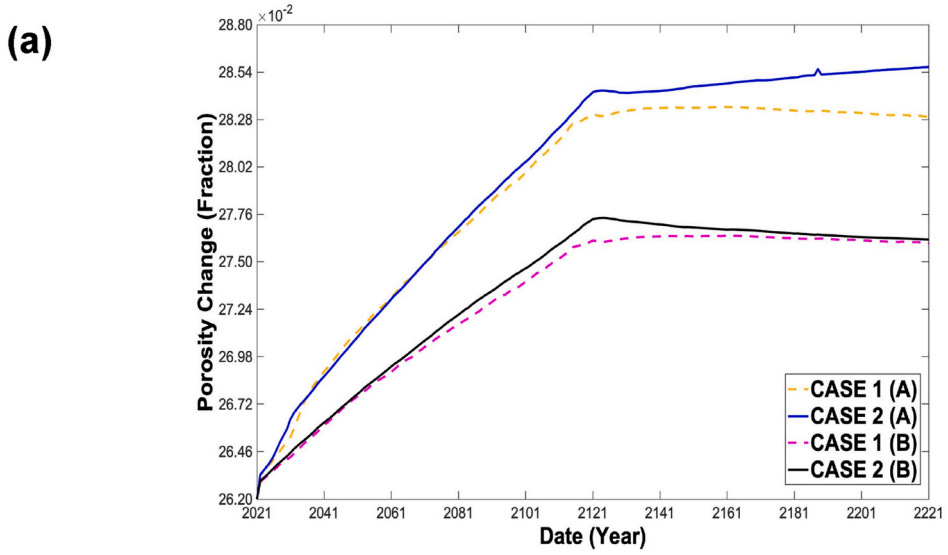

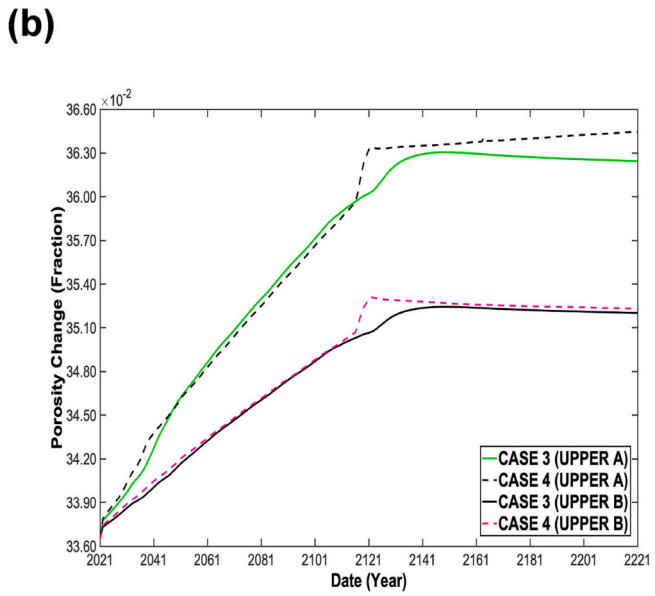

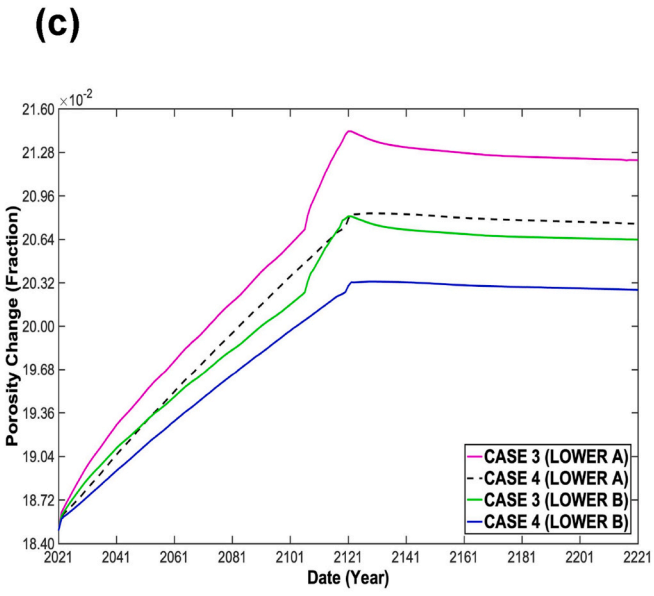

Fig. 10. (a) Shale inter-layer combined porosity change due to geomechanics, and geochemistry (A) and porosity change due to geomechanics module alone (B) for Cases 1 and 2 as a function of time. Upper (b) and lower (c) shale inter-layers combined porosity change due to geomechanics and geochemistry (A), and porosity change due to geomechanics module alone (B).

the large decline in pH reached an end at post-injection.

3.2. Cases 5 and 6

3.2.1. Flow

Fig. 20 shows x-z cross-sectional views, with a cut-off in y-direction at J = 10, of the simulated models. The horizontal, white dashed lines indicate the shale inter-layer location within the model to make it more apparent. Fig. 20(a) shows the distribution of the CO_2 plume before the reactivation of natural fractures, while Fig. 20(b) shows the CO_2 plume distribution after the reactivation of natural fractures.

3.2.2. Geomechanical processes

Fig. 21 shows the geomechanical behaviour of the inter-layers in Cases 5 and 6 over 200 years of simulated time. In particular, Fig. 21(a) shows the fracture pressure behaviour within the shale inter-layer as a function of time for Cases 5 and 6. It can be seen that the pressure increased rapidly during injection. Further, once the injection has stopped, a noticeable decrease in pressure was observed.

Fig. 21(b) shows that reduction of the effective stress occurred in both Cases because of an increase in the pore pressure introduced by the injection well. The stress reduction reached an end after the injection well was shut-in at 2121, and thereafter the effective stress started to build-up. Fig. 21(c) indicates that a seal uplift was caused by the injection into the reservoir for both Cases 5 and 6. The vertical movement is associated with the porosity change due to dilation and the compaction effect. Fig. 21(d) shows the increase in shale inter-layer permeability due to fracture re-activation. A fracture failure occurred due to the reduction in fracture effective normal stress to 3200 kPa. This resulted in fractures within the shale inter-layer opening up, and, thus, the fracture permeability increased, therefore, allowing the CO_2 to pass into the top overburden, as seen in Fig. 20(b).

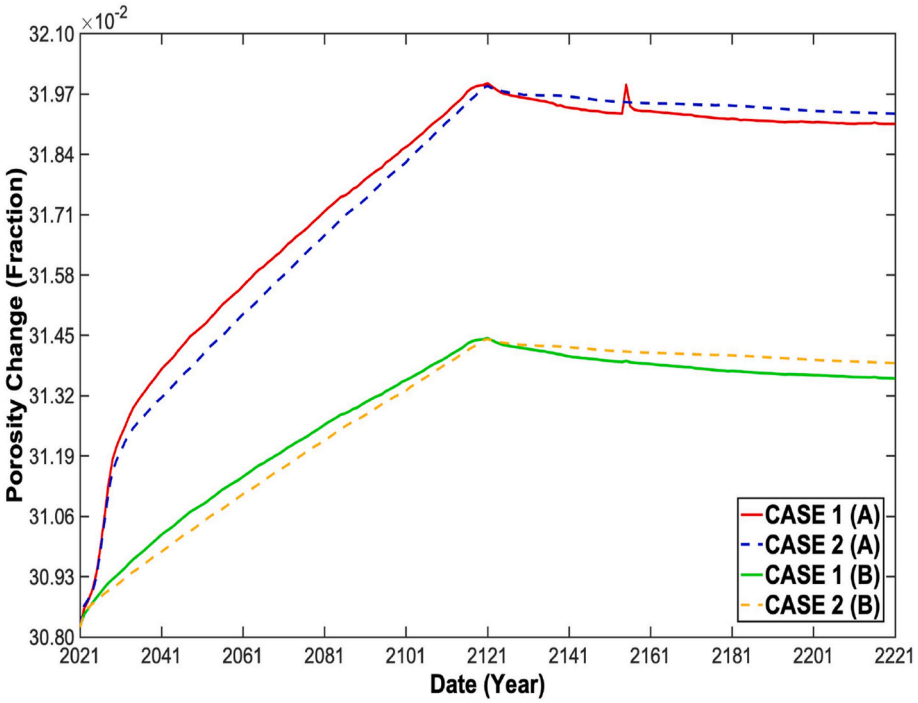

Fig. 11. The variation over time, for the sandstone layers which are directly below the shale inter-layer, of the porosity due to geomechanics, and geochemistry (A), and porosity change due to geomechanics module alone (B), for Cases 1 and 2.

4. Discussion

4.1. Cases 1-4

The coupling of the trio of flow, geomechanical and geochemical processes described above led to the unexpected behaviour in Cases 1 and 2, as will be discussed below. From Figs. 3–5, it was seen that the pore pressure increase within the shale inter-layers in Cases 1–4 during the first 100 years was significant due to supercritical (sc) CO_2 flooding within the closed boundary system. At the early stages of injection, the shale inter-layer, in Cases 1 and 3, exhibited a reduction in pressure because of the mechanical effects, such as dilation and bedding of the seal, which resulted in an increase in mean effective stress. Since $scCO_2$ is much more compressible than the brine when inside the pores of the shale inter-layer, thence the compressibility of the shale inter-layer mainly depends upon the $scCO_2$ pore concentration. Therefore, the $scCO_2$ compressibility within the inter-layer in Case 1 was larger compared to Case 2 (as shown in Fig. 15) which contributed towards causing a sudden reduction in pressure. Afterwards, the pore pressure increased progressively (the mean effective stress decreased) and the horizontal stress increased in Cases 1–4 due to lateral confinement as seen in Fig. 7(a–d). The shale inter-layer in Case 2 had a larger drop in the effective stress since the pore pressure was larger than that for the shale inter-layer in Case 1. This is due to the leakage that occurred via the shale inter-layer in Case 1, which resulted in a pressure relief for this shale inter-layer. Further, the simulation results indicate that pore pressure and mean effective stress have an inverse relationship within the shale inter-layers for Cases 1–4. Moreover, the change in the effective stress was less than the pore pressure due to the $scCO_2$ injection increasing the mean stress. This pressure started to gradually decline after the injection stopped due to the dominant solubility trapping of free and residual $scCO_2$ over a long time, since the main original source of pressure build-up was free $scCO_2$. However, over the long-term, pressure within the reservoir and shale inter-layer was maintained due to the buoyancy and capillary entry pressure at the plume boundaries. The pressure gradients caused by the change of the initial reservoir pressure due to the $scCO_2$ injection was the key driving force for plume migration in the direct vicinity of the injection well. As the CO_2 (Aq.) migrates further away from the injection well, the weaker the buoyancy forces become, and the greater is the influence of the advection on the flow direction.

Injection caused an overpressure to arise within the reservoir which, in turn, changed the vertical and horizontal stresses as shown in Fig. 7 (a–d), and this made the surrounding formation rocks, especially the region above the injector, to expand and push the inter-layer upwards (poroelastic expansion). The change in stresses resulted in the lower section of the shale inter-layer becoming horizontally compressed, and the upper section exhibited horizontal extension. Thus, the magnitude of ground deformation within shale inter-layers increased in Cases 1–4. The maximum vertical displacement of the shale inter-layer in Case 1 was 1.2 m, and was 1 m in Case 2. For Cases 3 and 4, the upper shale inter-layers had the largest increase with the vertical displacements of 1.3 m and 1.2 m, respectively, due to the upwards movement of CO_2 caused by the influence of the buoyancy force at the early stages of the simulation. Further, the vertical displacement of the lower shale inter-layers of Cases 3 and 4 increased by 0.4 m and 0.2 m in response to pressure build-up, respectively, as seen in Fig. 6(a) and (b). Therefore, by comparing Cases 1 and 2, it can be concluded that a thinner shale inter-layer will exhibit less uplift compared to a thicker shale inter-layer, which agrees with the results obtained by Iding and Ringrose (2009), and Lee et al. (2013). The extent of the vertical displacement depends upon several factors, including CO_2 injection rate, pressure build-up, the thickness of the seal, the porosity and permeability of the rock, and also the elastic modulus (Bao et al., 2013). The large increase in the vertical displacement in all Cases 1–6 was a result of the relatively low elastic modulus of 3×10^5 kPa defined for shale in the simulation.

The closed boundary condition also contributed to additional pressure build-up, limiting the CO_2 injection capacity, which was controlled by rock and fluid compressibility. The build-up of pore pressure under, and within, the shale interlayers, in both Cases 1 and 2, also contributed to increasing the seal integrity risk in terms of geomechanical changes within the shale inter-layer, such as vertical, and horizontal stresses,

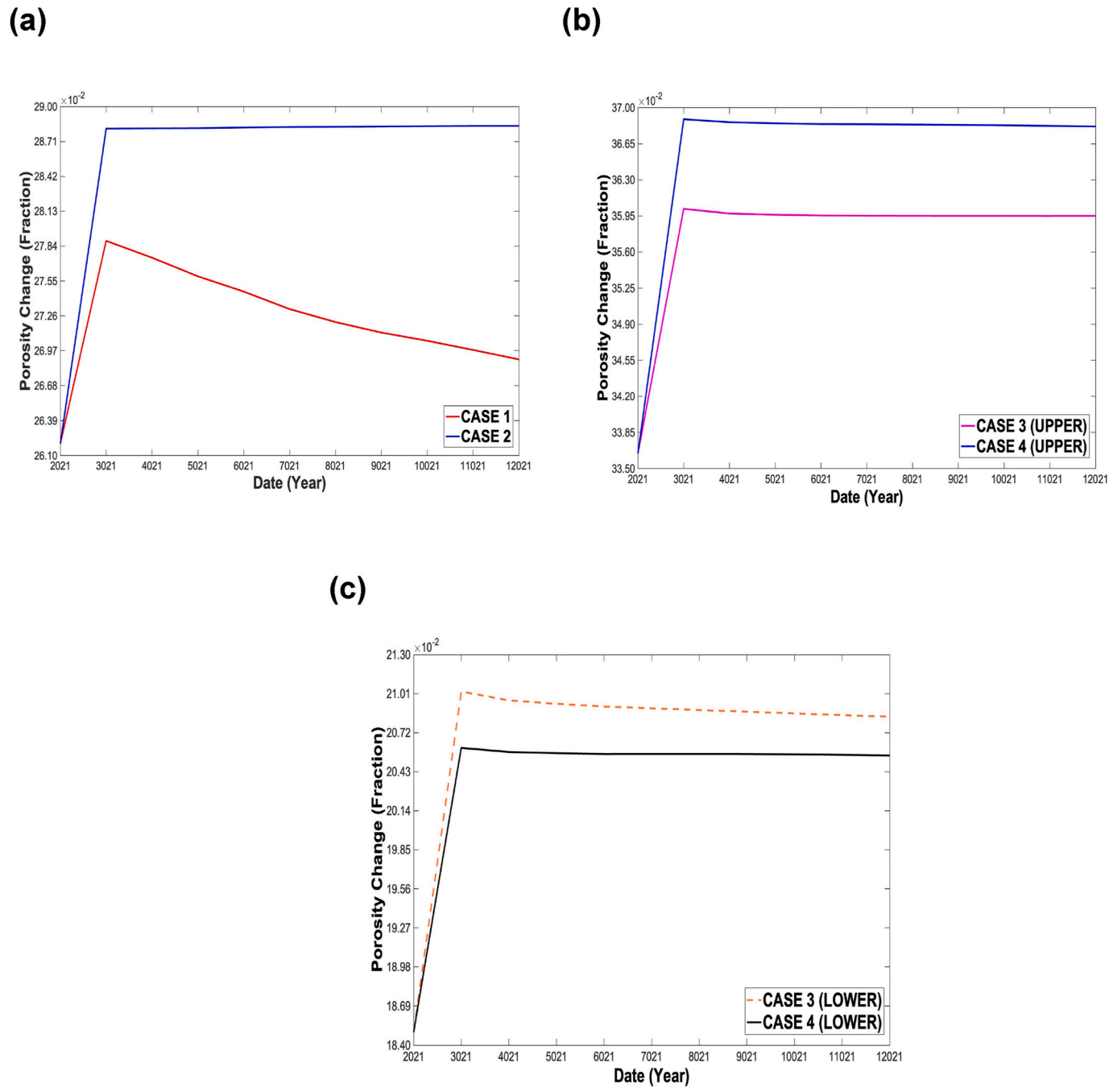

Fig. 12. Shale inter-layer porosity change for Cases 1 and 2 (a), and upper (b) and lower (c) shale inter-layers for Cases 3 and 4 during the 10,000 years of simulation.

deformation, volumetric strain, and effective stress, which then have a direct impact on the pore volume of the shale inter-layers. The porosity change after 100 years of injection was proportional to the pressure increase as seen in Figs. 3, 4 and 10. The porosity difference, between Cases 1 and 2, of the shale inter-layer caused specifically by geomechanical effects was minor during the latter 100 years of injection. However, at the early stages of injection, the shale inter-layer in Cases 1 and 3 (upper) exhibited a sudden reduction in porosity, as shown in Fig. 10(a&b), due to the poroelasticity effect caused by a decrease in pore pressure, vertical and horizontal stress, and volumetric strain, as seen in Figs. 3, 4, 7 and 8, respectively. Also, the porosity increased (due to pressure compressibility, and stress and strain change) during the injection period, for Cases 1 and 2 by 1.4% and 1.5%, respectively. Once the geochemical reactions were included, the overall porosity change, due to all processes including both geochemical and geomechanical, increased by 2.1% and 2.2% for Case 1 and 2 respectively as seen in Fig. 10(a). However, the shale inter-layer porosity in Case 2 kept increasing, compared to Case 1, after injection had stopped in 2121 due to the large accumulation of CO_2 within the former shale inter-layer, whereas CO_2 managed to escape the shale inter-layer in Case 1 which resulted in a relief in pore pressure (reduction in stress) within the shale, and, thus, the rise in porosity reduced.

Further, as seen from Fig. 9(a&b), in Case 1 the pore volume expanded due to geomechanical effects at the early stages of injection. In contrast, the pore volume in Case 2 remained unchanged during the injection period, but, at post-injection, the shale inter-layer in Case 2 exhibited a noticeable reduction in pore volume for a limited time, due to the elastoplastic effect resulting from dilation/compression which

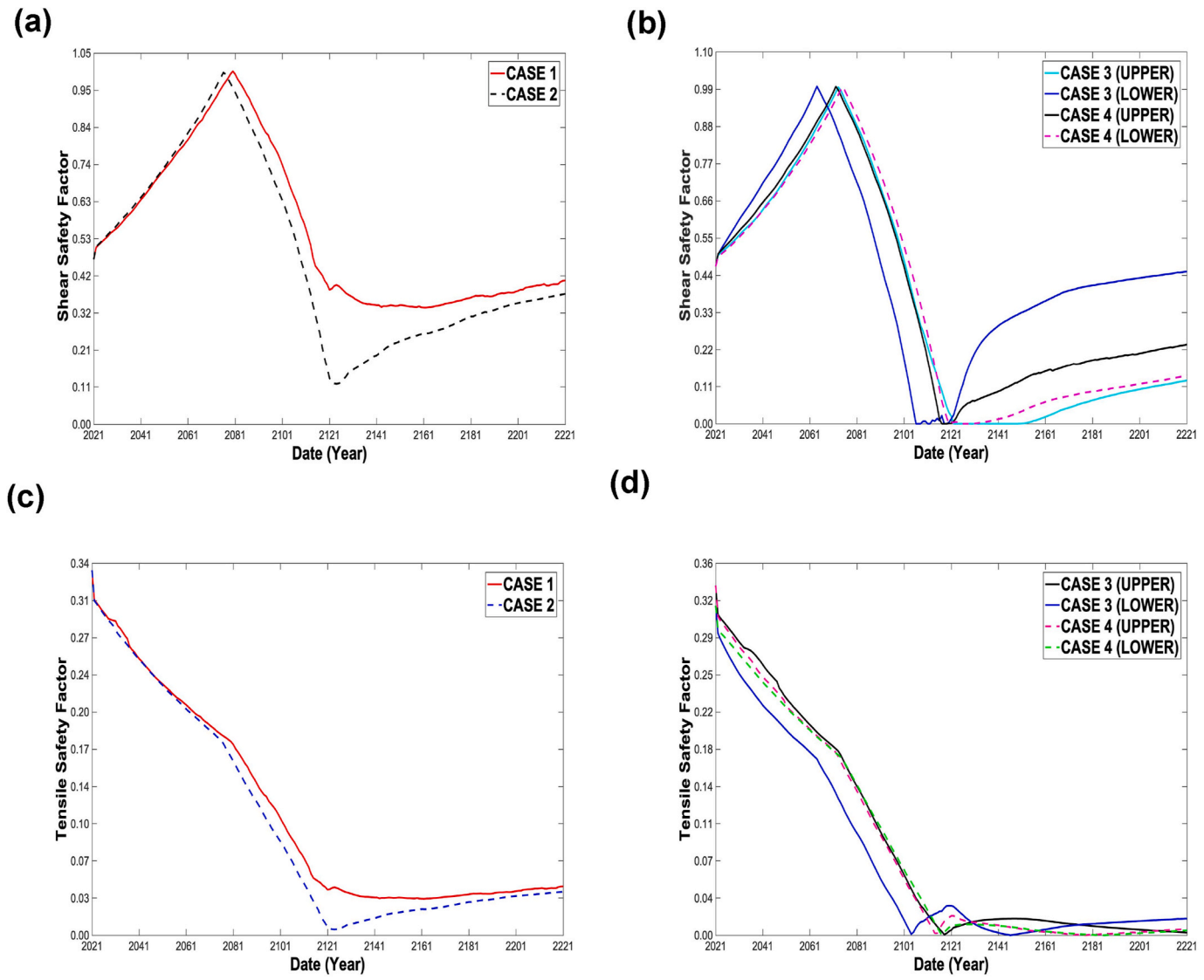

Fig. 13. Variation in shear (a&b) and tensile (c&d) safety factors with simulated time for Cases 1 and 2 (a&c) and Cases 3 and 4 (b&d).

was, in turn, controlled by external forces such as pore pressure (hydrostatic stress). The lower shale inter-layer in Case 3 had an increase in pore volume during injection, whereas the upper shale inter-layer in Case 4 manifested a reduction in pore volume at post-injection which was caused by geomechanical effects. Thus, the porosity of this inter-layer demonstrated a sudden increase for Case 3, but a sudden decrease for Case 4, as shown in Figs. 9(b) and 10(b&c). Therefore, monitoring the change in void spaces within the shale inter-layers, caused by geomechanics, will enhance the detection of a possible porosity change that could act as a pathway for the CO_2 to leak.

The shale inter-layers for Cases 1–4 were monitored during the first 200 years, and especially during the first 100 years of injection, to watch closely for the two failure mechanisms of shear and tensile failure. The cause of failure is governed by the mean effective stress, which has been demonstrated by both theoretical and experimental studies carried out by Biot (1941), Seyedi et al. (2009), and Vidal-Gilbert et al. (2009). Both types of failures are caused by the rise in pore pressure exceeding the initial pressure of the reservoir. In such a case, the effective stress reduces and once the pore pressure exceeds the least compressive principal stress, tensile failure will occur. In addition, shear failure will occur once the shear stress acting on the shale inter-layer exceeds it is shear strength. Shear failure can be reached within the inter-layers before exceeding the fracture pressure (Goodarzi and Settari, 2009). Cases 1 and 2 did not exhibit any failures, although, Case 1 was further away from shear and tensile failure than Case 2, and this was due to the pressure relief caused by the CO_2 leakage to the overburden in Case 1. In contrast, Cases 3 and 4 manifested both types of failures due to the large difference in the maximum and minimum stresses, but the periods of the incidence of these failures were very limited and did not have a noticeable impact on the porosity change such as to cause any major CO_2 seepage via the shale inter-layer to the overburden, as seen in Fig. 13 (a–d).

As can be seen from Fig. 17(a&b), in the short term, the incidence of free $scCO_2$ is significant during injection in Cases 1–4, but starts to reduce as the trapping mechanisms, such as capillary, solubility, and mineral trapping, become active. Additionally, the amount of dissolved CO_2 in brine continuously increases in Cases 1 and 2 due to the retardation of upwards CO_2 migration and therefore increased contact with brine caused by the shale inter-layer. The shale inter-layer reduced the vertical CO_2 velocity significantly for Cases 1–4 due to their ultra-low permeability. Capillary trapping decreased upon the stoppage of injection. Case 1 had the lowest trapped CO_2 compared to Cases 2–4. At the end of the observation period, Cases 1–4 showed that structural and dissolution trapping become the main trapping mechanisms. Moreover, the amount of brine salinity within the shale inter-layer in Case 2, at the early stages, was larger than in Case 1, whereupon CO_2 solubility in the

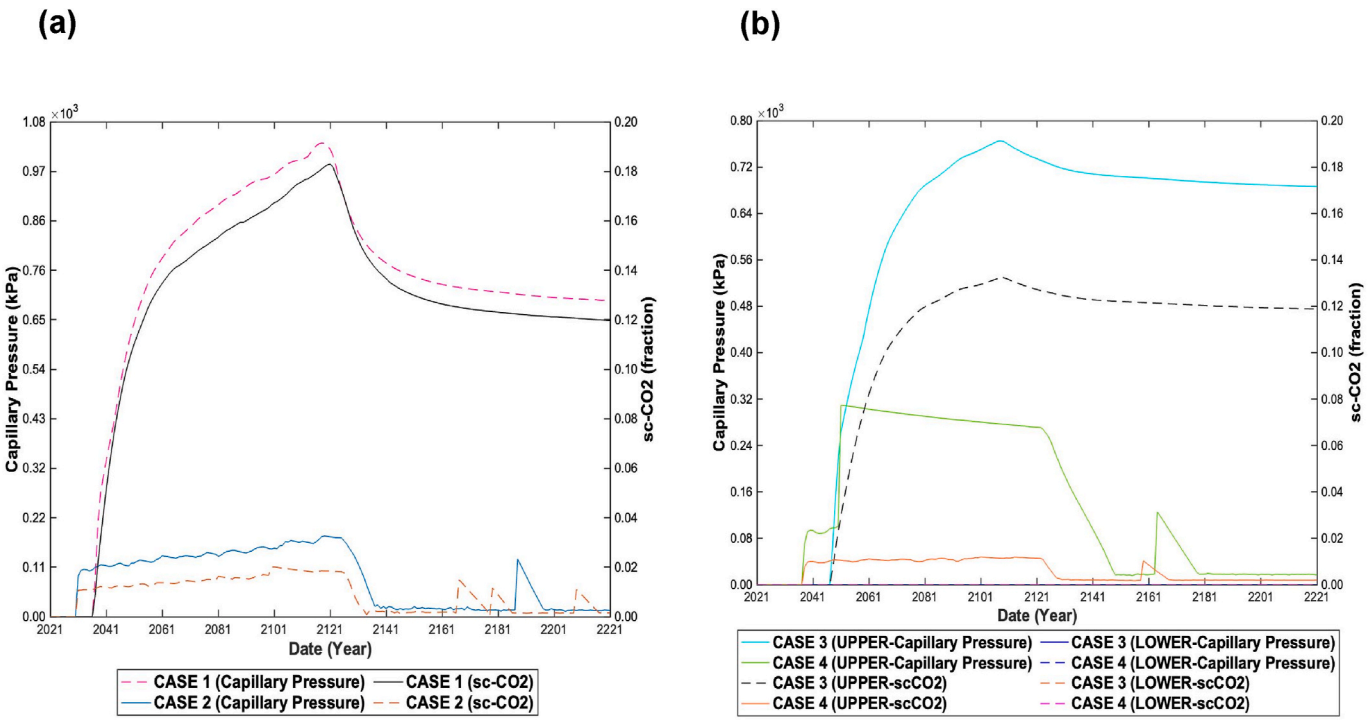

Fig. 14. Water-Gas capillary breakthrough pressure behaviour of shale inter-layer for Cases 1 and 2 (a), and upper, and lower shale inter-layers for Cases 3 and 4 (b), as a function of time.

brine decreased as the salinity of the brine increased, as shown in Fig. 19 (a&b). This finding agreed with previous work (De Silva et al., 2015; Ahmadi and Chapoy, 2018; Duan and Sun, 2003). Thus, the amount of CO_2 present in the supercritical phase at field scale in Case 2 was larger than in Case 1, as seen in Fig. 17(a). This was because the salinity in Case 1 kept increasing, whereas, in Case 2, it started to decline, which caused the amount of the dissolved CO_2 in Case 1 to reduce, but in Case 2 to increase, as shown in Figs. 17(a) and 19(c).

Upon injection, $scCO_2$ interacts with the resident brine and produces carbonic acid, which decomposes into H^+ and HCO_3^- ions. As a result, the pH of the brine drops within the shale inter-layers for Cases 1–4, as seen in Fig. 19(a&b). However, this drop in pH within the shale inter-layers for Cases 1–3 is brought to an end because of calcite dissolution which consumes H^+. In contrast, the brine pH of the upper shale inter-layer in Case 4 exhibited a further reduction because of the increase in the CO_2 solubility due to a reduction in salinity, as shown in Fig. 19 (b&d).

As was mentioned earlier, the CO_2 plume was monitored for 10,000 years in a long-term sequestration simulation. The large dissolution of $scCO_2$ and the reduction in brine pH, together with the excess of calcium and bicarbonate ion concentrations after the CO_2-brine-rock interaction, are a result of the decomposition of carbonic acid that was formed by $scCO_2$ dissolution, which promoted the fast-reactive mineral (calcite) dissolution within the shale inter-layers for Cases 1–4 as can be seen in Fig. 18(d)

In addition, two main parameters, namely low permeability and high capillary entry pressure of the shale inter-layer, will constrain the penetration of the $scCO_2$ and it must overcome the entry capillary pressure in order to enter the layer. The shale inter-layer capillary breakthrough pressure was monitored for Cases 1–4 to evaluate the amount of $scCO_2$ and CO_2 (aq.) that managed to enter the shale inter-layer during the 100 years of injection. Due to the shale inter-layer thickness difference between Case 1 and 2, the initial penetration of both $scCO_2$ and CO_2 (aq.) into the thick shale inter-layer was at a later stage in Case 1 compared to the thin shale inter-layer in Case 2, as seen in Fig. 14(a). This allowed more $scCO_2$ to accumulate under the thick shale inter-layer in Case 1 compared to Case 2. Hence, this meant that the layers of sandstone which are directly under the shale inter-layer in Case 1 underwent a large build-up of pore pressure compared to Case 2 as shown in Fig. 3(b). This resulted in a larger increase in the stresses, and porosity, of sandstone layers, in Case 1, when compared to Case 2 (as shown in Fig. 11). Therefore, the minimum pressure needed to initiate the displacement of brine in the shale inter-layer (breakthrough pressure) was partially reached at the seal/reservoir interface. Therefore, the shale inter-layer in Case 1 had the largest increase, of 1000 KPa, in capillary breakthrough pressure, with 18% of $scCO_2$ managing to invade the shale inter-layer compared to Case 2, which had a lower build-up to just 173 kPa and, thence, only 2% of $scCO_2$ managed to enter this shale inter-layer as shown in Fig. 14(a). The capillary pressure was not fully exceeded, and, thus, the maximum amount of $scCO_2$ that invaded the shale inter-layer was limited. In Cases 3 and 4, it can be seen, during the early injection period, that, while the upper shale inter-layers exhibited partial capillary breakthrough compared to the lower shale inter-layers, this was due to the upwards migration of $scCO_2$ which resulted from the buoyancy force. However, the amount of $scCO_2$ that had managed to enter upper inter-layer was still limited as shown in Fig. 14(b).

The larger amount of $scCO_2$ that managed to penetrate within the thicker brine saturated shale inter-layer in Case 1 meant more chemical reactions occurred, which contributed towards causing more calcite dissolution compared to Case 2. From Fig. 18(a–c), the precipitation and dissolution of other minerals such as albite-low (albite forms at low temperatures), chalcedony, muscovite, kaolinite, K-feldspar, and siderite were insignificant within the shale inter-layers for Cases 1–4 because of the low reaction rates and insensitivity to pH change.

The shale inter-layer porosity declined over the longer-term of the simulation in Case 1, whereas, in Case 2, the porosity remained steady in the longer-term as shown in Fig. 12 (a). This was because the decrease in the porosity by 2%, resulting from certain mineral reactions (precipitation of chalcedony), in Case 1 and Case 2 remained stable as seen in Fig. 18 (a). Additionally, the long-term reduction in the pressure and vertical displacement (uplift) resulted in a decrease in the shale inter-

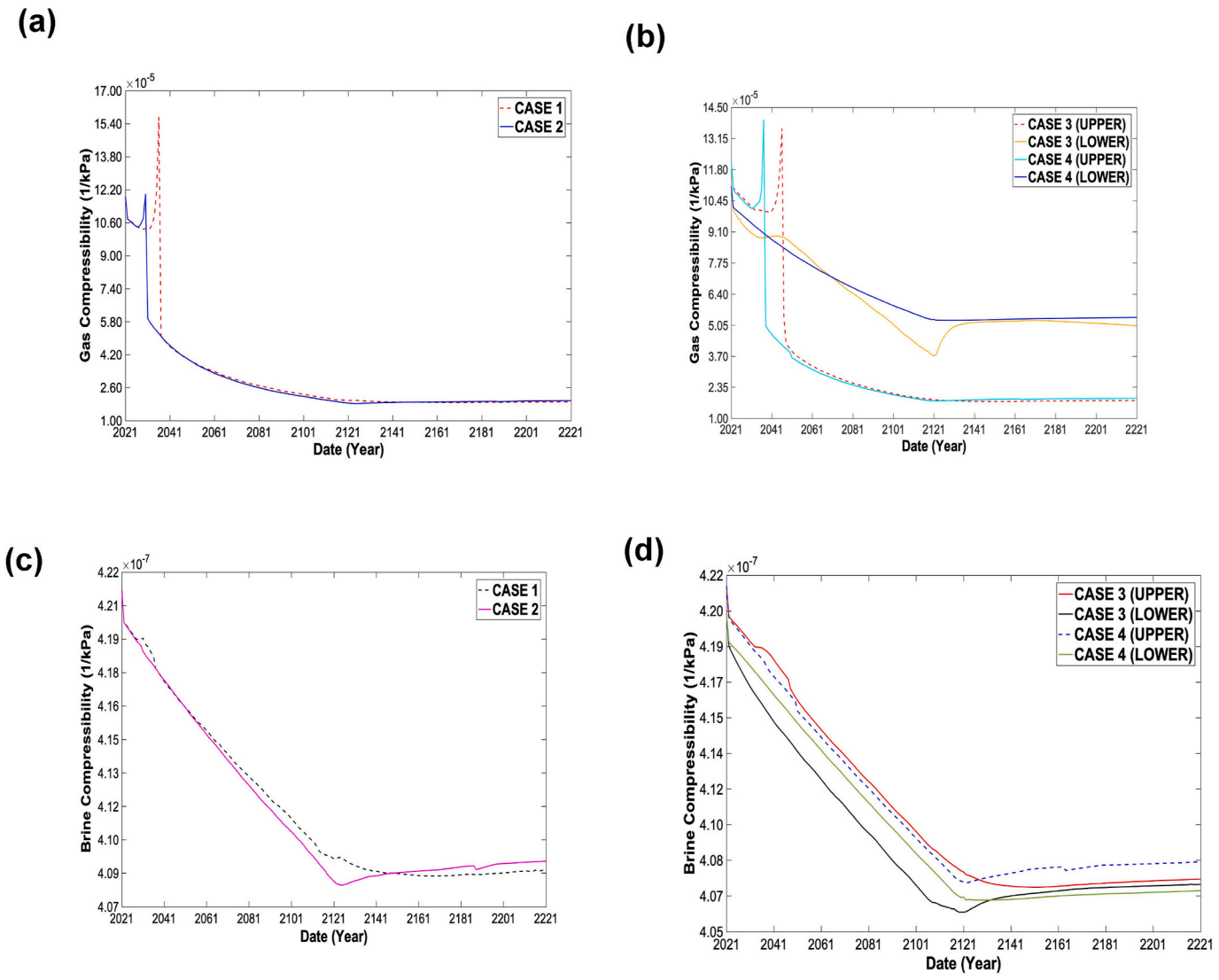

Fig. 15. CO_2 (a&b) and brine (c&d) compressibility change over time within the shale inter-layer for Cases 1 and 2 (a&c), and the upper and lower shale inter-layers for Cases 3 and 4 (b&d).

layer porosity. This decrease was more significant in Case 1, compared to Case 2, which contributed towards a porosity reduction.

The CO_2 movement in the reservoir continued for several years, due to the presence of the pressure and density gradient. Once the CO_2 has dropped to residual saturation, the CO_2 will not move due to buoyancy and advective forces. Thus, it can only dissolve into the brine and be transported diffusively. Despite, the high capillary entry pressure (capillary seal) of the shale inter-layer, this will not prevent molecular diffusion from occurring due to both the inter-layer pores being saturated with brine and there being some large porosity value regions due to the presence of heterogeneity in porosity within the shale inter-layers in Cases 1–4. Moreover, the nature of the shale inter-layers, as being thin, meant that the $scCO_2$ could invade the entire barrier in a short period, and not just the base of the seal layer as would have been the case for thicker caprocks. Therefore, the CO_2 concentration gradient between the plume at the surface and pore fluid of the inter-layer was significant which enhanced the CO_2 transported via diffusion. This is similar to the findings of Xiao et al. (2020) where CO_2 migrated through the Morrow Shale faster via diffusion in the aqueous phase, compared to capillary flow in the supercritical phase. In contrast, much prior research has mainly focused on thick caprocks, such as the study carried out by Gaus et al. (2002) which investigated molecular diffusion through 100 m of homogenous Nordland shale caprock. In that case, the penetration of $scCO_2$ into the caprock was only at the base of the seal. Hence, then, the large thickness of the caprock slowed down the diffusion flux, and the molecular diffusion effect was minor. Therefore, the molecular diffusion mechanism for leakage is usually ignored in simulations (Chadwick et al., 2008). However, the results described here suggest that it is important for plume migration through thin inter-layers and baffle seals.

The leakage of the CO_2 plume in Case 1 first started with CO_2(aq.) entering the 3 m shale inter-layer, as a result of diffusion, and, after several years of continuous injection, only then did $scCO_2$ capillary invasion from the reservoir to the shale inter-layer take place (Chadwick et al., 2008; Gaus, 2010). However, the 0.3 m shale inter-layer in Case 2 managed to hold back the CO_2(aq.) from migrating to the overburden. The sealing efficiency of the 3 m shale inter-layers in Case 1 was not

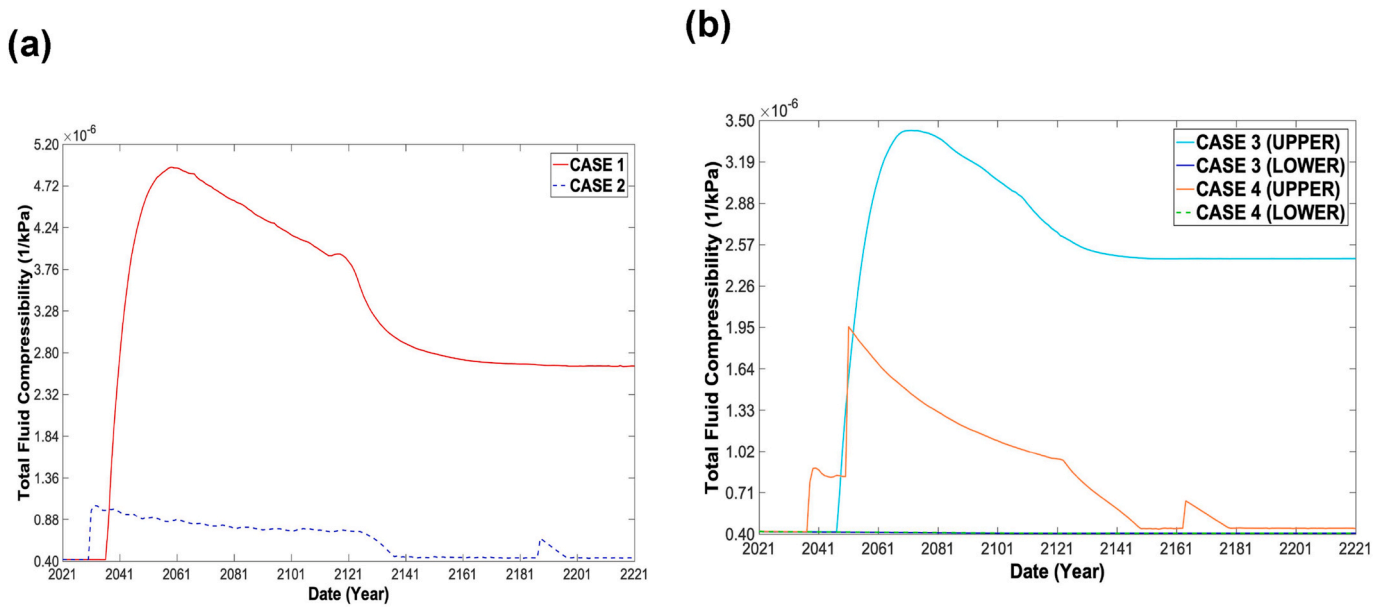

Fig. 16. Total fluid compressibility of shale inter-layer for Cases 1 and 2 (a), and the upper and lower shale inter-layers for Cases 3 and 4 (b), as a function of time.

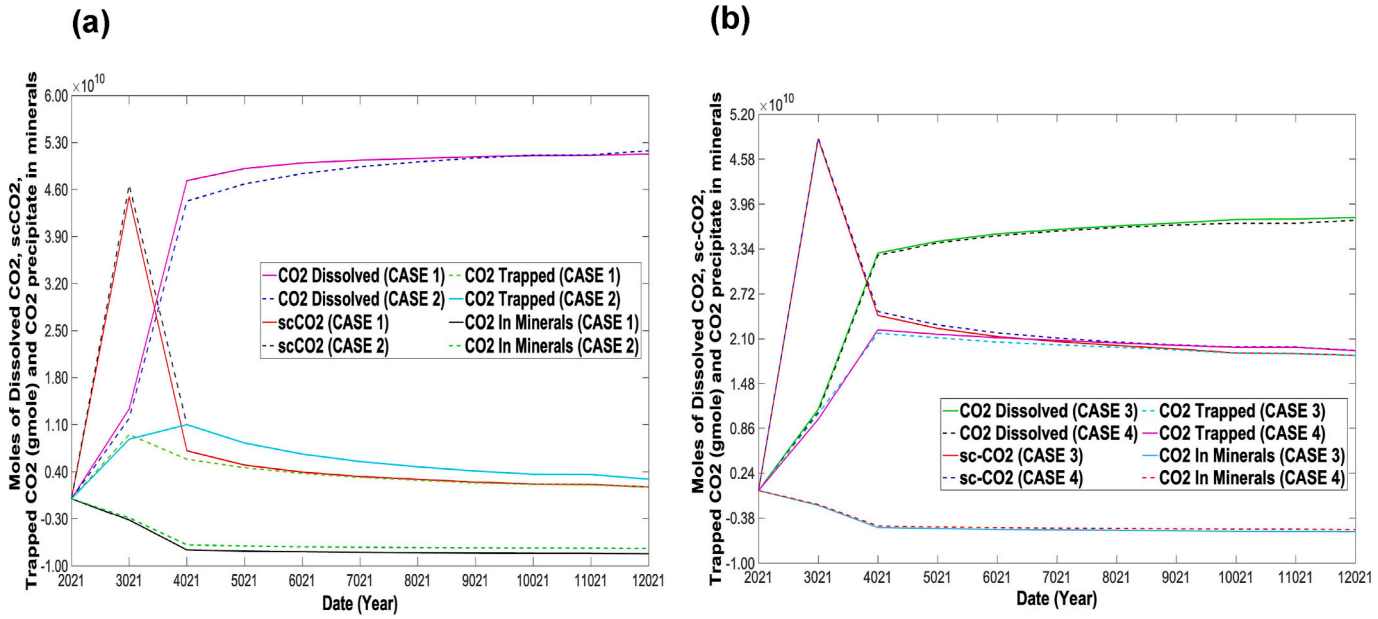

Fig. 17. Variation over time of the number of moles of CO_2 present in various states, including dissolved into native brine, as $scCO_2$, as CO_2 (aq.), as CO_2 precipitated in minerals, and as CO_2 trapped at field scale, for Cases 1 and 2 (a), and 3 and 4 (b).

good enough to prevent the CO_2 (aq.) from leaking to the overburden, since 20% of the CO_2(aq.) managed to escape through the shale inter-layer, as seen in Fig. 2 (a). The results obtained here contrast with the outcomes of the study conducted by Hou et al. (2012), where they concluded that a thinner caprock would cause more leakage to the overburden compared to a thick caprock. This discrepancy with the findings presented here was due to this previous work not considering different geometries of seal, such as inter-layers, and also not treating the total complexity of the system, including fully-coupled flow, geochemical, and geo-mechanical processes, and thus only using an over-simplified simulation scheme not involving all three physical processes together. Additionally, the results in Fig. 2 (a&b) have shown that the injection between two different thicknesses of shale inter-layers in Cases 3 and 4 lead to a good sealing effectiveness compared to Case 1.

As more $scCO_2$ invades into the brine-saturated seal this will lead to more chemical reactions, such as mineral precipitation and dissolution, occurring, which enhances the diffusive breakthrough time (Busch et al., 2008). Furthermore, the amount of dissolved CO_2 is the key factor in terms of influencing the CO_2 diffusion rate (Ho et al., 2005), since a high concentration of bicarbonate in the aqueous phase is the driving force for the $scCO_2$ to be dissolved in the native brine (Mandalaparty, 2012). It is noted that Case 1 had a more significant concentration of bicarbonate compared to Case 2. This resulted in the amount of $scCO_2$ dissolved being larger in Case 1 compared to 2. The reaction and solubilisation of the calcite mineral within the thick shale inter-layer in Case 1 was significant compared to shale inter-layer in Case 2. In addition, the lower brine salinity level within the inter-layer in Case 1, compared to Case 2, enhanced the diffusion by increasing the CO_2 solubility. Therefore, the dissolved CO_2 (in brine) concentration gradient at the reservoir/inter-layer boundary increased, which drove the molecular

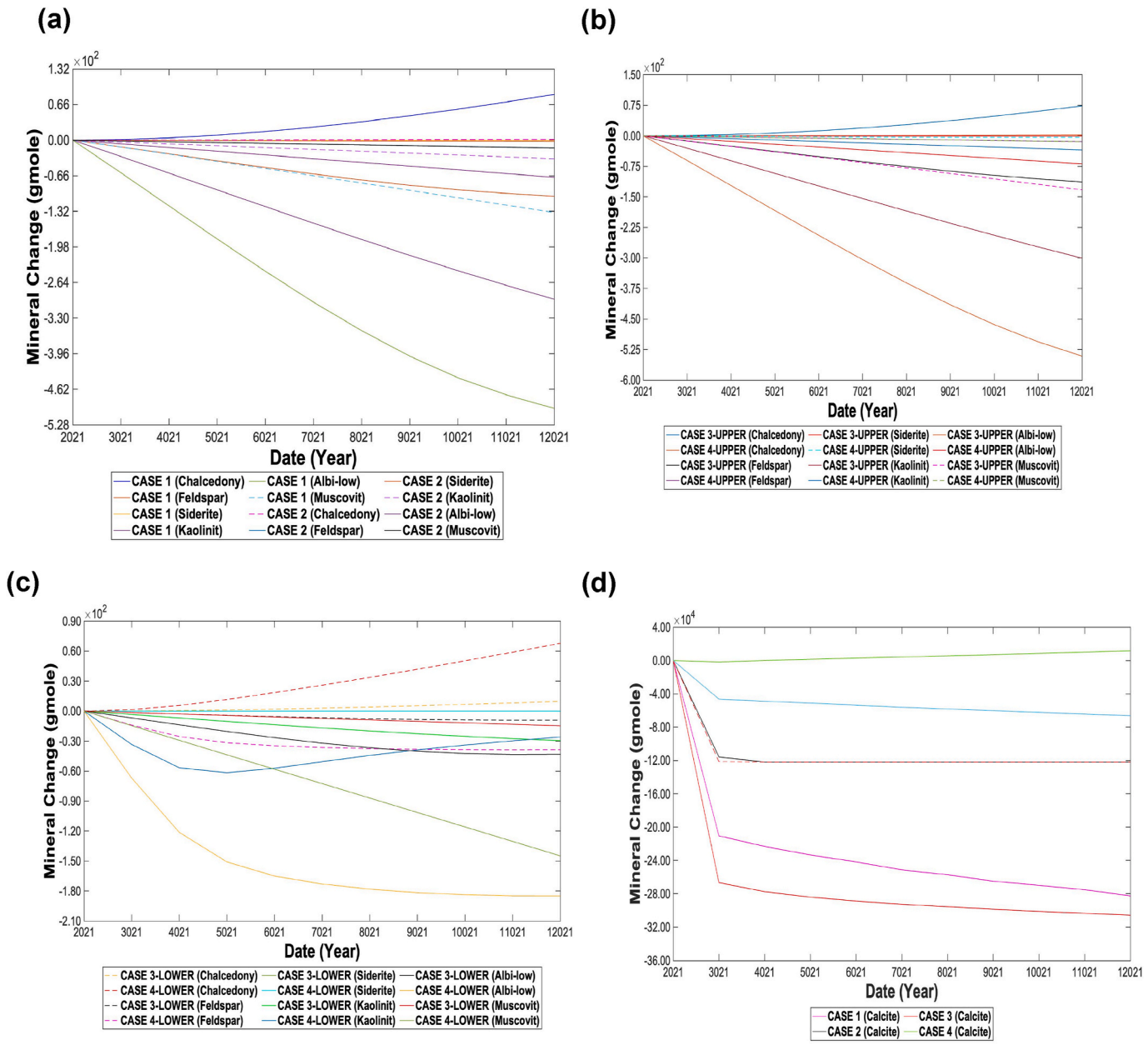

Fig. 18. Variation in mineral content within the shale inter-layers for Cases 1–4 (a–d) as a function of time. Upper and lower refer to the respective two shale layers in Cases 3 and 4.

diffusion of the non-wetting fluid to the upper storage repository, through the fluid filled, interconnected porous network of the inter-layer, which in turn directly increased the diffusion flux, and, thus, enhanced diffusive loss of dissolved CO_2 through water-saturated pore spaces within the thick shale inter-layer. As a result, CO_2 (aq.) managed to migrate upwards towards the overburden in Case 1. As was mentioned previously, the shale inter-layer in Case 1 exhibited larger uplift, compared to Case 2, and also a higher effective stress in Case 1, compared to 2, which enhanced the shale inter-layer surface area. Therefore, the diffusion process was accelerated by increasing the rock surface area.

The leakage that occurred, via the shale inter-layer in Case 1, resulted in a reduction in the total fluid compressibility within the inter-layer during injection compared to Case 2, which had no leakage as shown in Fig. 16(a). In contrast, Cases 3 and 4 manifested a lower increase in total fluid compressibility within the shale inter-layer due to the lower $scCO_2$ invasion into the inter-layers, as seen in Fig. 16(b). Furthermore, the shale inter-layer in Case 1 had the largest total fluid compressibility (brine and CO_2) due to the shale inter-layer being thicker than the shale in Case 2. Hence, the shale storage capacity is larger. Additionally, the compressibility contrast between both fluids ($scCO_2$ and brine, as shown in Fig. 15) was a result of the large pore compressibility of shale inter-layers for Cases 1–4.

The more effective local seal provided by the thinner (0.3 m) shale inter-layer (Case 2) compared to the thicker (3 m) inter-layer (Case 1) is, maybe, counter-intuitive, but results when all coupled processes, including all of geochemical, geomechanical, petrophysical heterogeneity, hysteresis, capillary pressure, and diffusion, were included in one model. The unexpected leakage pattern arose from a series of events mentioned above, and summarised as follows. First, the pore volumes of the interlayer and nearby reservoir were relatively more expanded by larger geomechanical effects in Case 1 than Case 2. The large change in stresses, arising from the injection process, caused a greater increase in the vertical displacement of the thick inter-layer compared to the thin

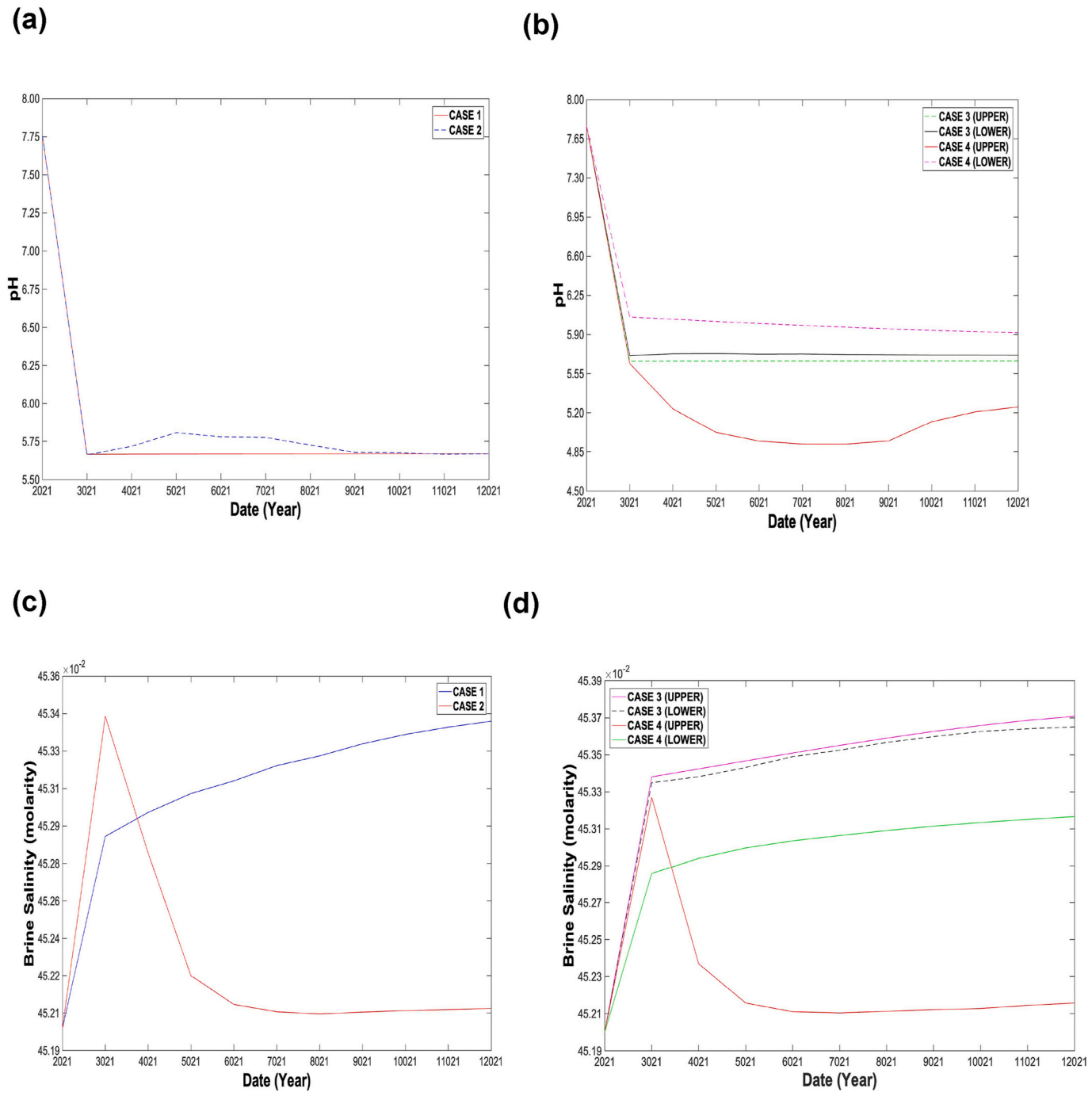

Fig. 19. Variation in brine pH (a&b) and brine salinity (c&d) within the shale inter-layers as a function of time for Cases 1–4.

inter-layer, which contributed to the diffusive loss by enhancing the overall interlayer porosity due to the larger flexion. In addition, the porosity of the sandstone reservoir region abutting the interlayer increased by a greater amount in Case 1 (with the thicker shale inter-layer) due to the larger pressure difference between the initial reservoir and pore pressure. This, in turn, caused a larger accumulation of CO_2 beneath the ultra-low permeability thick inter-layer, compared to with the thinner inter-layer. This large accumulation resulted in the achievement of a higher capillary breakthrough pressure within the thick inter-layer, allowing more $scCO_2$ to enter the thicker inter-layer, that was initially saturated with brine. As a consequence, more extensive chemical reactions could happen within the thick inter-layer. These included a change in pH, larger solubility of CO_2 and a decrease in brine salinity, and also faster calcite dissolution, along with more reactions of other minerals. All of these changes led to an enhancement of the levels of dissolved CO_2 at the reservoir/inter-layer boundary, which meant, thereby, there was a larger concentration gradient, this, in turn, increased the diffusive loss via the thick inter-layer. This ultimately led to the substantially higher leakage via the thick inter-layer, to the overburden, than occurred for the thinner layer (as seen in Fig. 2). This study showed how the combination of a more complete complement of coupled physical processes in the simulation can lead to unexpected findings, that might, otherwise, not be predicted by simpler models.

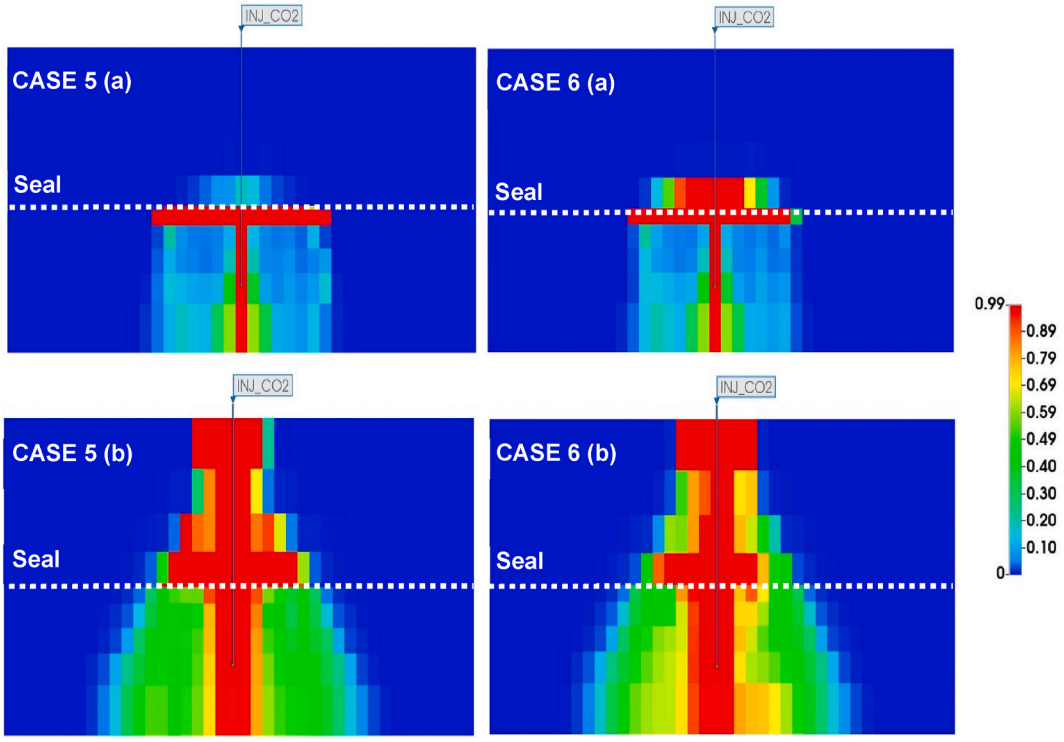

Fig. 20. The radial distribution of CO_2 plume behaviour after 50 years of injection of before reactivation (a) and after reactivation of natural fractures (b) at 100 years of injection. The colour scale bar represents the global mole fraction of 'CO_2' (mole fraction of 'CO_2' in aqueous phase + mole fraction of 'CO_2' in gas phase).

4.2. Cases 5 and 6

Induced natural fractures arose in the 3 m and 0.3 m shale inter-layers in Cases 5 and 6, respectively. At the early stage of injection, before the reactivation of fractures occurred, the escape of CO_2 to the overburden resulted from diffusive loss via the inter-layer. The dilation effect had caused the increase in the uplift of the shale inter-layers in both Cases 5 and 6 which enhanced the diffusion process, as shown in Figs. 20(a) and Fig. 21(c). It can be seen that the amount of leaked CO_2 arising after the reactivation of fractures was larger than before the reactivation process, as seen in Fig. 20(b). The reactivation of the natural fractures was caused by the high fluid pressure, rather than the geochemical reaction, since it occurred at the early stages of injection, where reaction was less significant. The reactivation occurred due to the reduction in the normal effective stress sufficiently (3200 kPa) such that failure had taken place, as can be seen in Fig. 21(a&b). In turn, the fractures having opened, this caused the initially low permeability of the shale inter-layer to increase to 35 mD, thereby allowing the CO_2 to penetrate the overburden, as shown in Fig. 21(d).

The integrity of the shale inter-layers is violated by a geomechanical mechanism such as reactivation of induced fractures. Where Cases 5 and 6 displayed the impact of the re-activation of fractures was in the primary effect of reducing the sealing efficiency by enabling and enhancing, the CO_2 buoyancy-driven, upwards migration via the shale inter-layer and then it continuing towards the surface. The leakage in both Cases was a result of two leakage mechanisms, namely initially through diffusive loss, followed by reactivated fractures. The presence of re-activated fractures within the shale inter-layers created permeable pathways. Hence, the effective permeability of the CO_2 phase is enhanced and made the capillary sealing (in terms of preventing the upwards migration of CO_2) ineffective, since the capillary invasion occurs via the large, interconnected pores within the shale inter-layers. Additionally, diffusive loss via the microfractures and matrix of the shale inter-layer was at a noticeably fast rate in both Cases. In contrast, a previous study conducted by Johnson et al. (2004), has shown that the movement of the CO_2 (via the 25 m fractured shale caprock from Sleipner field) due to diffusion was slow, because of the large thickness of the seal, the homogenous porosity, and the particular set of minerals that were used in the simulation.

In Cases 1–6, the combination of chemical and mechanical states is a function of time. The mechanical and chemical effects on the reservoir and the shale inter-layers, respectively, are spatially and temporally different. Spatially, the mechanical effect has a larger impact on both regions (sandstone and shale), whereas the chemical impact was less during the first 100 years of injection. Temporally, the mean effective stress, vertical displacement, volumetric strain, and total normal vertical and horizontal stresses significantly changed at the early stage of injection. For instance, the mean effective stress was reduced immediately from day 1 of the simulation, but later, negligible change was observed. In contrast, chemical precipitation/dissolution kept changing at a constant rate throughout the simulation period.

4.3. Sensitivity analysis

To further assess the unusual leakage that occurred in Case1, but not in Case 2, the same simulations were run again for Cases 1 and 2, but with different relative permeability curves, capillary entry pressure, and a semi-opened boundary condition instead of a closed boundary. Both sets of runs resulted in the same outcome as the previous finding, where the unusual leakage occurred in Case 1, but not for Case 2. However, the amount of the leakage of CO_2 was less, in comparison to the previous results from Case 1, because the semi-opened boundary condition

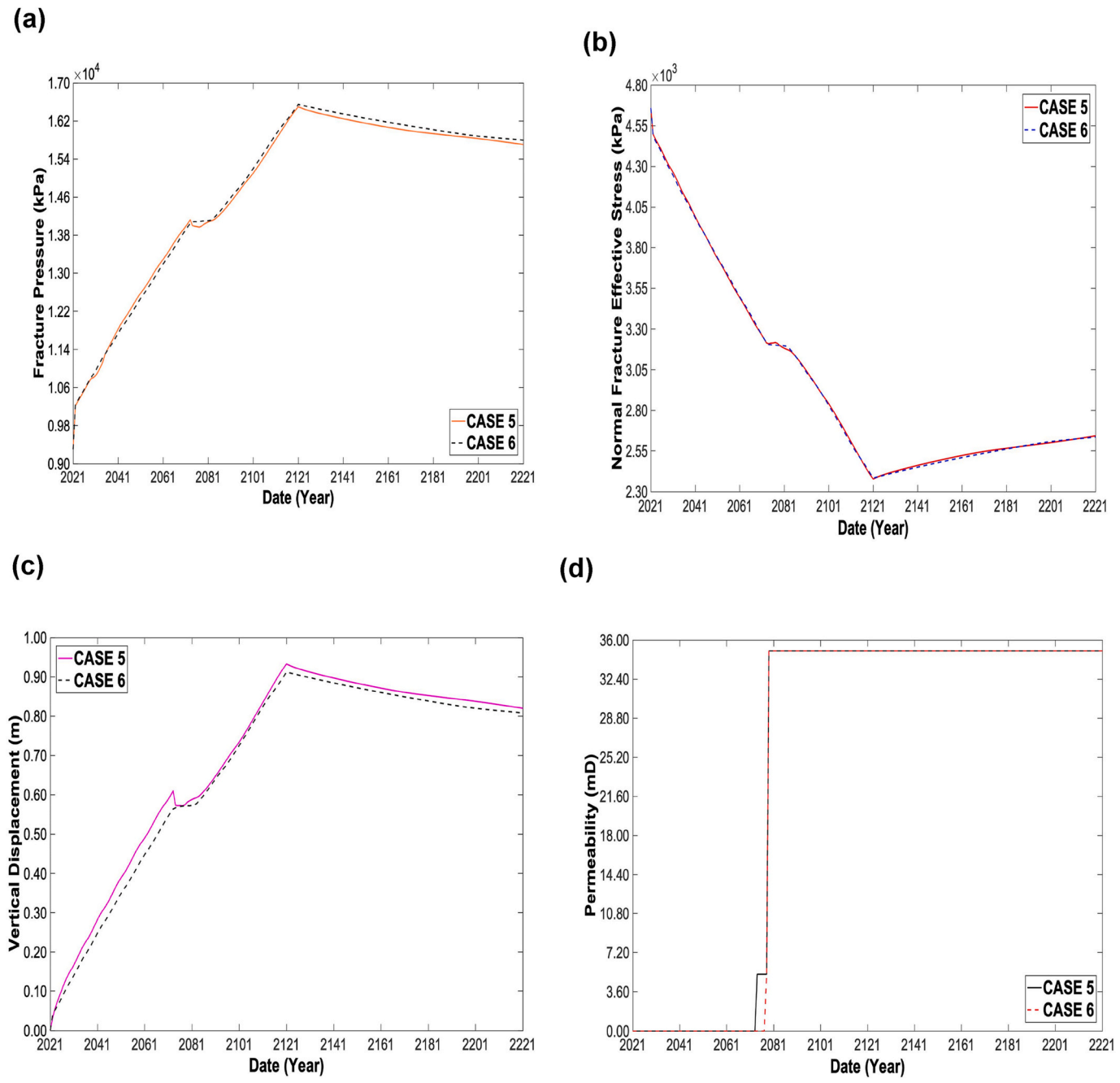

Fig. 21. Variation over time of the fracture pressure behaviour (a), effective stress of the natural fractures (b), vertical displacement (c), and permeability of the shale inter-layer (d) for Cases 5 and 6.

allowed some relief in pressure. This in turn, meant that the over-pressure was insufficient to overcome the capillary sealing and the leakage only occurred due to diffusive loss through the shale inter-layer. Further, the simulations for Cases 1 and 2 were also run with simulation grids of overall size 50,000 blocks. It was also found that the same results occurred, whereby the 3 m thick shale layer leaked, whereas the 0.3 m thick layer did not, thereby suggesting the result was not just due to the size of the simulation grid.

5. Conclusion

The integrity of the caprock is a key factor in providing safe and reliable geological storage. Despite the importance of understanding caprock integrity using a combination of natural accumulations, field studies, experimental, and numerical modelling, it has received relatively minor attention in past research efforts, due to the lack of accurate information with regard to caprock properties and thicknesses. This has led to the numerical simulations to monitor the seal integrity being conducted including only limited properties, which leads to unreliable

results. For instance, including geomechanics properties, but ignoring geochemical, petrophysical heterogeneity, capillary sealing, and diffusion processes. In this study, a field-scale reactive transport model was built with fully coupled hydrogeological, geochemical, and geomechanical information from the Sleipner gas field using the CMG-GEM software simulation tool to simulate six different Cases, to analyse and monitor the CO_2 plume movement and the possibility of leakage mechanisms occurrence under different conditions.

The results have shown that the thinner shale inter-layer in Case 2 was more efficient in terms of reducing the CO_2 leakage to the overburden compared to the thicker shale inter-layer in Case 1. Additionally, Cases 3 and 4 results indicated that the injection between two shale inter-layers will reduce the possibility of CO_2 leakage via the seal compared to Case 1, and, hence, it will enhance the sealing efficiency. Furthermore, the re-activation of natural fractures in shale inter-layers has been shown to cause a serious impact on the sealing efficiency for both Cases 5 and 6. The stress-strain quickly propagated laterally within the injection zone, together with fluid pressure (limited by the injection duration). The pressurization resulted in vertical expansion which, in turn, caused ground surface deformation of both reservoir and inter-layers and changes in the stress field. These induced changes are, proportional to the increase in pore pressure, reservoir pressure difference, and geometry and geomechanical properties (such as compressibility) of the reservoir and also, surrounding sediments. Pore pressure and mean effective stress were inversely proportional, and, also, CO_2 solubility and brine salinity had an inverse relationship. The largest capillary breakthrough pressure was exhibited in Case 1, which, in turn, resulted in 18% of $scCO_2$ moving from the reservoir into the inter-layer. Afterwards, 20% of CO_2(Aq.) managed to escape the inter-layer and migrated to the overburden by diffusion. Both tensile and shear failures occurred only for such a short time as to not cause any major impact on the porosity and permeability of the shale inter-layers. The change in geochemistry and geomechanics did not make a large change in porosity within the inter-layer over the 10,000 years for Cases 1–4. Further, the dominant leakage mechanisms that have occurred, via the shale inter-layers to the overburden, are diffusive loss for Case 1, whereas, for Cases 5 and 6, it was diffusive loss followed by reactivation of natural fractures. Based on the sensitivity analysis, it can be confirmed that the leakage that occurred via the thick shale inter-layer, but not via the thin inter-layer, is not limited to a fixed condition but can occur under a diverse range of different conditions. For example, using different capillary entry pressures, relative permeabilities, and boundary conditions.

Credit author statement

Ali Alsayah: Conceptualization, Methodology, Formal analysis, Investigation, Writing - Original Draft **Sean Rigby:** Conceptualization, Resources, Writing - Original Draft, Writing - Review & Editing, Supervision, Funding acquisition.

Declaration of competing interests

The authors declare that they have no known competing financial interests or personal relationships that could have appeared to influence the work reported in this paper.

Data availability

The data that has been used is confidential.

Acknowledgements

AA and SPR thank the GeoNetZero CDT and University of Nottingham for funding of a PhD studentship. We also thank CMG for assistance with the use of the GEM software.

Appendix A1

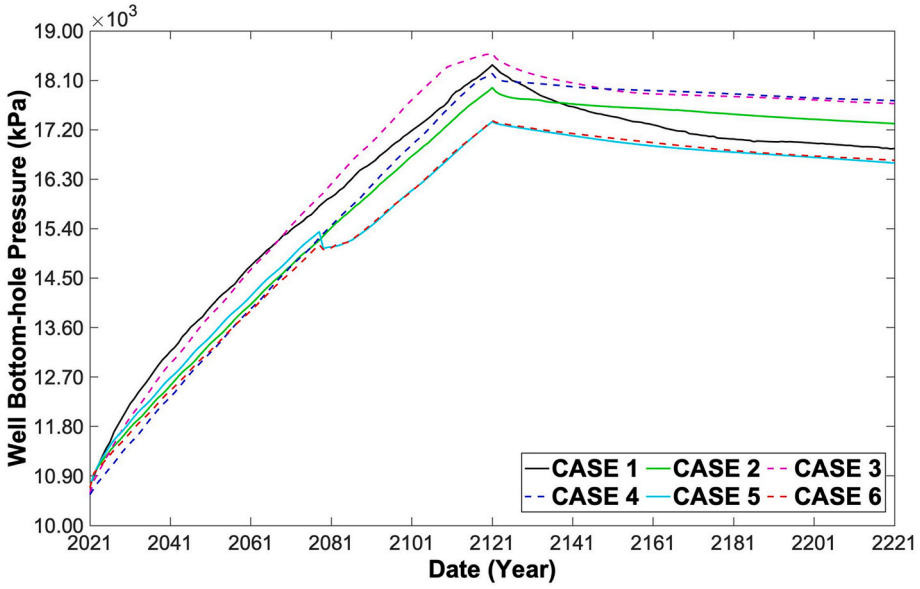

Fig. A1. Well bottom hole pressure as a function of time for Cases 1–6.

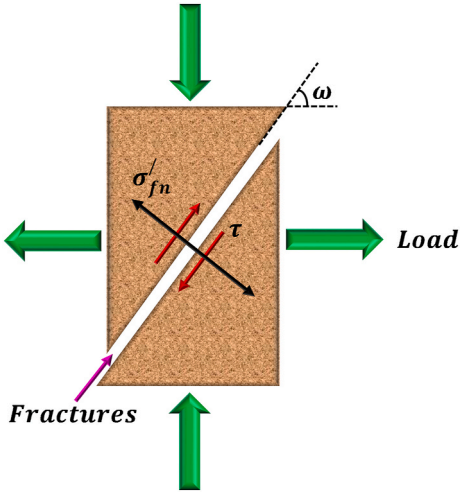

Fig. A2. Fracture in a block subject to loads, and definition of stresses and fracture orientation, where σ'_{fn} is the effective normal stress, τ is the fracture shear stress, and ω is the angle of orientation (modified from Tran et al., 2009).

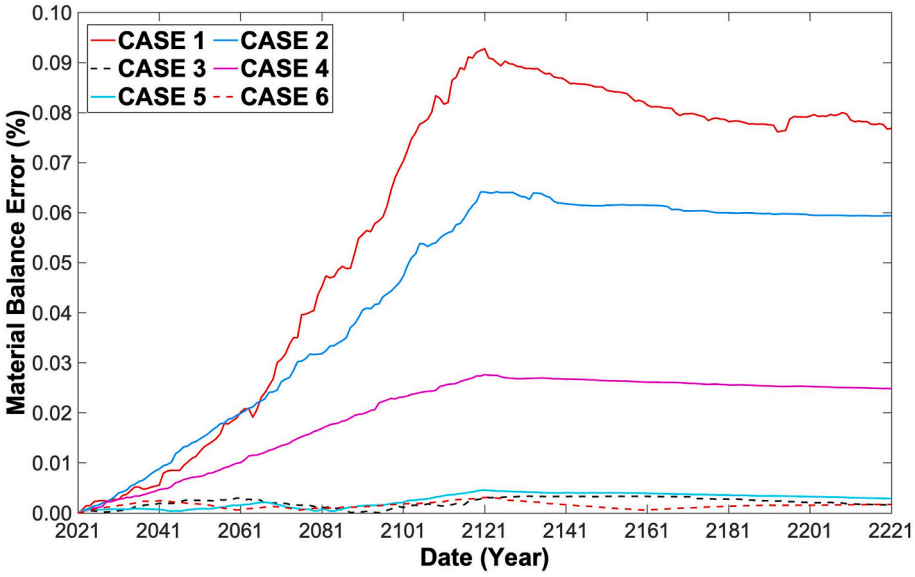

Fig. A3. Overall material balance error for fluids over course of simulations

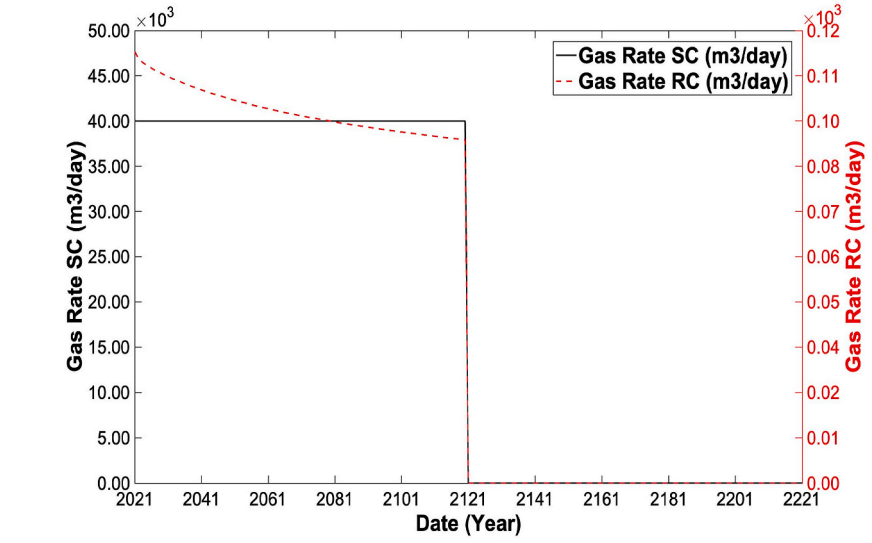

(a)

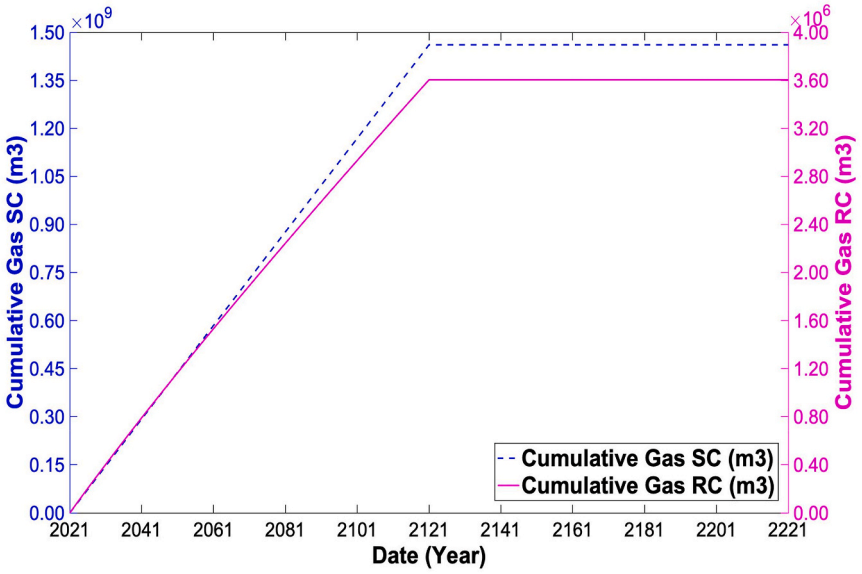

(b)

Fig. A4. (a) Well injection rate at surface condition (SC) and reservoir condition (RC) as a function of time for Cases 1–6. (b) Cumulative gas at surface condition (SC) and reservoir condition (RC) as a function of time for Cases 1–6.

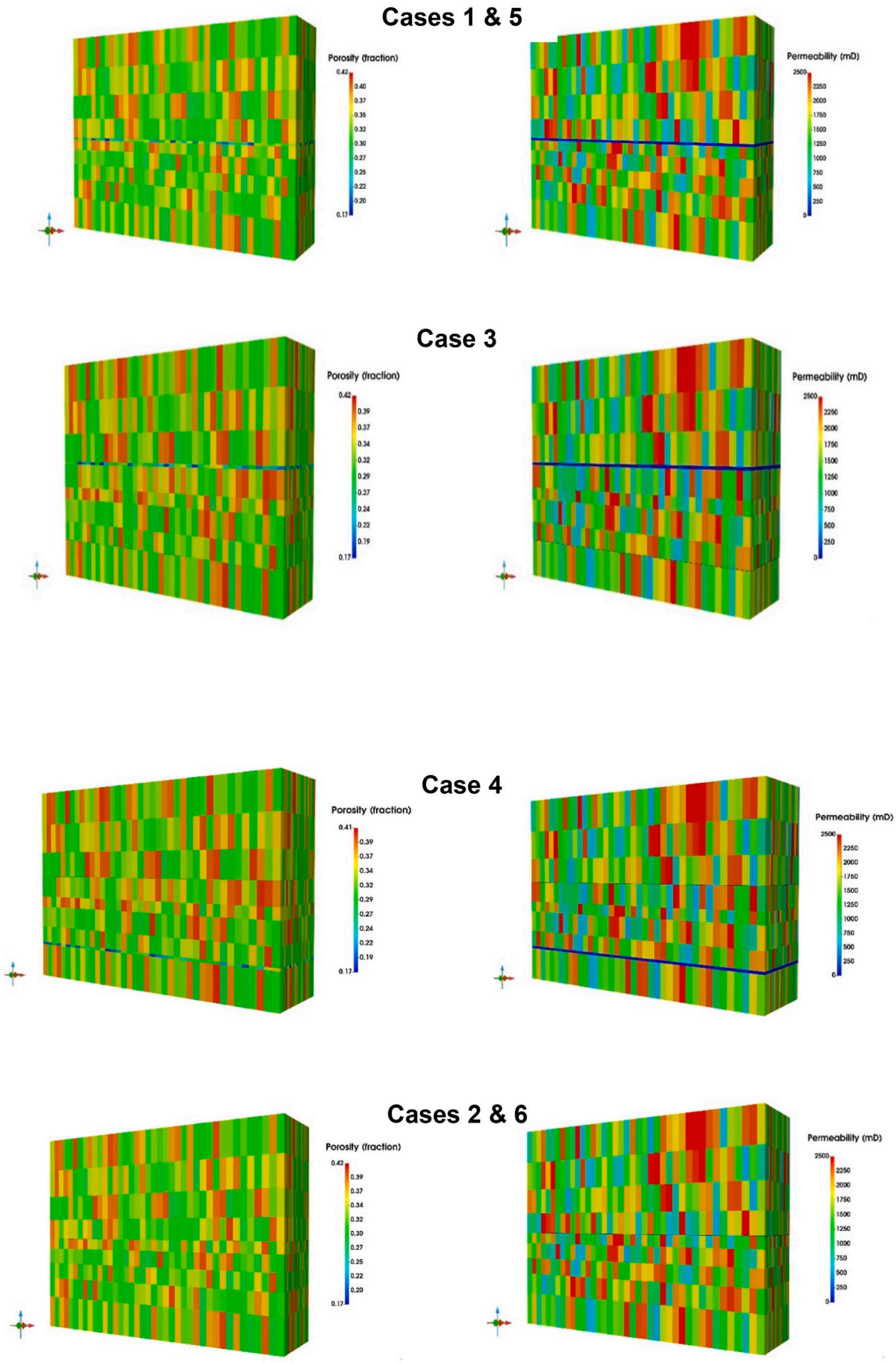

Fig. A5. Distribution of vertical permeability and porosity in the heterogeneous 3D media using Gaussian geostatistical simulation for Cases 1–6.

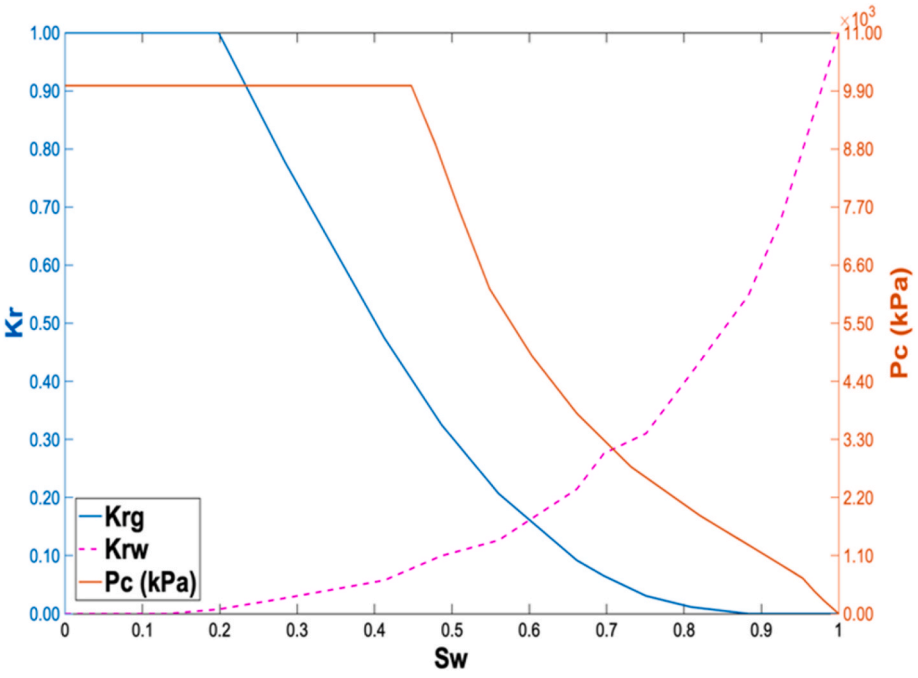

Fig. A6. Relative permeability and capillary pressure of Nordland Shale as a function of water saturation that have been used for Cases 1–6 (Williams et al., 2018).

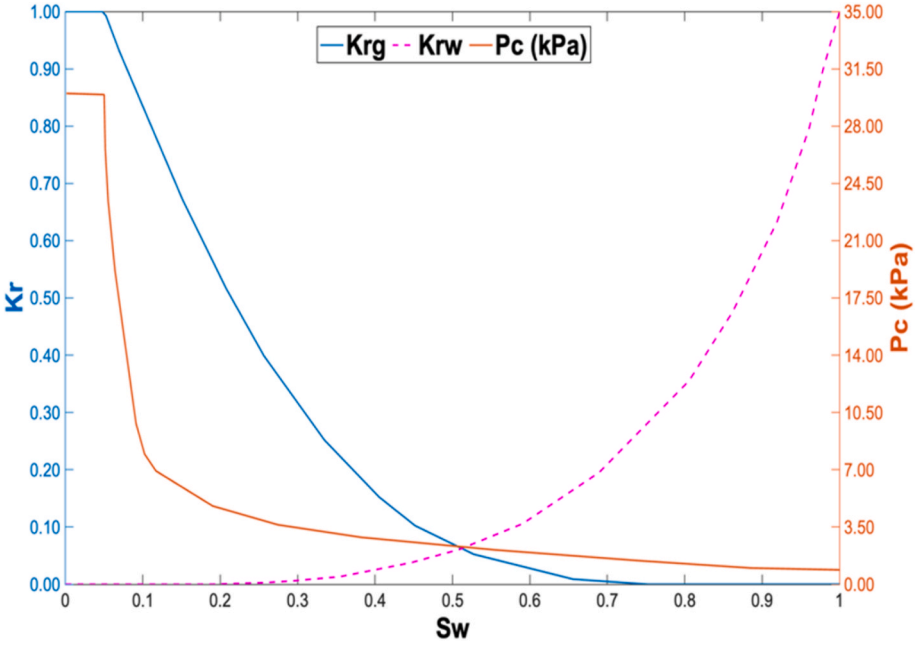

Fig. A7. Relative permeability and capillary pressure of Utsira Sand as a function of water saturation that have been used for Cases 1–6 (Williams et al., 2018).

References

Agartan, E., Cihan, A., Illangasekare, T.H., Zhou, Q., Birkholzer, J.T., 2017. Mixing and trapping of dissolved CO2 in deep geologic formations with shale layers. Adv. Water Resour. 105, 67–81.

Ahmadi, P., Chapoy, A., 2018. CO2 solubility in formation water under sequestration conditions. Fluid Phase Equil. 463, 80–90.

Amann, A., Waschbüsch, M., Bertier, P., Busch, A., Krooss, B.M., Littke, R., 2011. Sealing rock characteristics under the influence of CO2. Energy Proc. 4, 5170–5177.

Audigane, P., Gaus, I., Pruess, K., Xu, T.. A LONG TERM 2D VERTICAL MODELLING STUDY OF CO2 STORAGE AT SLEIPNER (NORTH SEA) USING TOUGHREACT. https://www.researchgate.net/publication/237288757_A_LONG_TERM_2D_VERTICAL_MODELLING_STUDY_OF_CO2_STORAGE_AT_SLEIPNER_NORTH_SEA_USING_TOUGHREACT.

Bao, J., Xu, Z., Lin, G., Fang, Y., 2013. Evaluating the impact of aquifer layer properties on geomechanical response during CO2 geological sequestration. Comput. Geosci. 54, 28–37.

Biot, M.A., 1941. General theory of three-dimensional consolidation. J. Appl. Phys. 12, 155–164.

Bitrus, P.R., Iacopini, D., Bond, C.E., 2016. Defining the 3D geometry of thin shale units in the Sleipner reservoir using seismic attributes. Marine and Petroleum Geology 78, 405–425.

Busch, A., Alles, S., Gensterblum, Y., Prinz, D., Dewhurst, D.N., Raven, M.D., Stanjek, H., Krooss, B.M., 2008. Carbon dioxide storage potential of shales. Int. J. Greenh. Gas Control 2, 297–308.

Cavanagh, A.J., Haszeldine, R.S., 2014. The Sleipner storage site: capillary flow modeling of a layered CO2 plume requires fractured shale barriers within the Utsira Formation. Int. J. Greenh. Gas Control 21, 101–112.

Chadwick, R., Arts, R., Bernstone, C., May, F., Thibeau, S., Zweigel, P., 2008. Best Practice for the Storage of CO2 in Saline Aquifers - Observations and Guidelines from the SACS and CO2STORE Projects, vol. 14. British Geological Survey Occasional Publication, pp. 1–267.

CMG-GEM, 2020. GEM Users Guide. Computer Modeling Group, Canada.

Dean, R.H., Gai, X., Stone, C.M., Minkoff, S.E., 2003. A comparison of techniques for coupling porous flow and geomechanics. In: Proceedings of SPE Reservoir Simulation Symposium. Houston, texas USA, 3-5 February 2003 (SPE 79709).

De Silva, G.P.D., Ranjith, P.G., Perera, M.S.A., 2015. Geochemical aspects of CO2 sequestration in deep saline aquifers: a review. Fuel 155, 128–143.

Duan, Z., Sun, R., 2003. An improved model calculating CO2 solubility in pure water and aqueous NaCl solutions from 273 to 533 K and from 0 to 2000 bar. Chem. Geol. 193, 257–271.

Elenius, M.T., Gasda, S.E., 2013. Convective mixing in formations with horizontal barriers. Advances in Water Resources 62, 499–510.

Farajzadeh, R., Ranganathan, P., Zitha, P.L.J., Bruining, J., 2011. The effect of heterogeneity on the character of density-driven natural convection of CO2 overlying a brine layer. Advances in Water Resources 34, 327–339.

Fleury, M., Pironon, J., Le Nindre, Y.M., Bildstein, O., Berne, P., Lagneau, V., Broseta, D., Pichery, T., Fillacier, S., Lescanne, M., Vidal, O., 2011. Evaluating sealing efficiency of caprocks for CO2 storage: an overviewof the Geocarbone Integrity program and results. Energy Proc. 4, 5227–5234.

Gasda, S.E., Wangen, M., Bjørnarå, T.I., Elenius, M.T., 2017. Investigation of caprock integrity due to pressure build-up during high-volume injection into the Utsira formation. Energy Proc. 114, 3157–3166.

Gaus, I., 2010. Role and impact of CO2–rock interactions during CO2 storage in sedimentary rocks. Int. J. Greenh. Gas Control 4, 73–89.

Gaus, I., Azaroual, M., Czernichowski-Lauriol, I.. Reactive Transport Modeling of Dissolved CO2 in the Cap Rock Base during CO2 Sequestration (Sleipner Site, North Sea). https://www.sintef.no/globalassets/project/ik23430000-sacs/publications/gaus_etal_carbonseqiiconf.pdf.

Gilman, J.R., Kazemi, H., 1983. Improvements in simulation of naturally fractured reservoirs. SPE J. 23, 695–707.

Global CCS Institute, 2020. Global CCS Institute welcomes the 20th and 21st large-scale CCS facilities into operation [Online]. Available: https://www.globalccsinstitute.com. Accessed 1 May 2021.

Goodarzi, S., Settari, A.T., 2009. Geomechanical Modelling and Analysis Wabamun Area CO2 Sequestration Project (WASP). Institute for Sustainable Energy, Environment and Economy.

Green, C., Ennis-King, J., 2009. Effect of vertical heterogeneity on long-term migration of CO2 in saline formations. Transport Porous Media 82, 31–47.

Gutierrez, M., Prassetyo, S.H., 2017. Modeling of the coupled hydro-mechanical response of geological sequestration reservoirs due to CO_2 injection. Geotechnical Frontiers GSP 280, 678–687.

Haddad, M., Sepehrnoori, K., 2017. Development and validation of an explicitly coupled geomechanics module for a compositional reservoir simulator. J. Petrol. Sci. Eng. 149, 281–291.

Ho, A., Fokker, P.A., Orlic, B., 2005. Caprock Integrity of Deep Saline Reservoirs and Coupled Processes. Netherlands Institute of Applied Geosciences, Utrecht.

Holloway, S., Chadwick, R.A., Kirby, G.A., Pearce, J.M., Gregersen, U., Johannessen, P. N., Kristensen, L., Zweigel, P., Lothe, A., Arts, R., 2000. Saline Aquifer CO2 Storage (SACS) - Final Report: Work Area 1 Geology: BGS Report.

Hou, Z., Murray, C., Rockhold, M., 2012. Evaluating the impact of caprock and reservoir properties on potential risk of CO2 leakage after injection. Environ. Earth Sci. 66.

Iding, M., Ringrose, P., 2009. Evaluating the impact of fractures on the long-term performance of the in Salah CO2 storage site. Energy Proc. 25, 2021–2028.

IPCC, 2005. IPCC Special Report on Carbon Dioxide Capture and Storage. Available: https://www.ipcc.ch/report/carbon-dioxide-capture-and-storage/. Accessed 1 May 2021.

Johnson, J., Nitao, J., Morris, J., 2004. Modeling the Long-Term Isolation Performance of Natural and Engineered Geologic CO2 Storage Sites.

Khan, S., Khulief, Y.A., Al-Shuhail, A.A., 2020a. Effects of reservoir size and boundary conditions on pore-pressure buildup and fault reactivation during CO_2 injection in deep geological reservoirs. Environ. Earth Sci. 79, 294.

Khan, S., Khulief, Y.A., Al-Shuhail, A.A., Bashmal, S., Iqbal, N., 2020b. The geomechanical and fault activation modeling during CO2 injection into deep minjur reservoir, eastern Saudi arabia. Sustainability 12, 9800.

Lee, J., Min, K.-B., Rutqvist, J., 2013. Probabilistic analysis of fracture reactivation associated with deep underground CO2 injection. Rock Mech. Rock Eng. 46, 801–820.

Lindeberg, E., Van Der Meer, B., Moen, A., Wessel-Berg, D., Ghaderi, A., 2000. SACS Task 2: fluid and core properties and reservoir simulation. In: The Saline Aquifer CO2 Storage (SACS) Project: SINTEF Report.

Lothe, A.E., Zweigel, P., 1999. Saline Aquifer CO2 Storage (SACS). Informal Annual Report 1999 of SINTEF Petroleum Research Result in Work Area 1. Reservoir Geology: SINTEF Report.

Mandalaparty, P., 2012. Reaction Chemistry in Carbon Dioxide Sequestration. PhD. Dissertation, University of Utah.

Mohammed, A., Ekoja, G.A., Adeniyi, A.A., Hassan, A.B., 2012. Modelling Long Term CO2 Storage in Saline Aquifers. International Journal of Applied Science and Technology 2, 53–62.

Noy, D.J., Holloway, S., Chadwick, R.A., Williams, J.D.O., Hannis, S.A., Lahann, R.W., 2012. Modelling large-scale carbon dioxide injection into the Bunter Sandstone in the UK Southern North Sea. International Journal of Greenhouse Gas Control 9, 220–233.

Ojala, I.O., 2011. The effect of CO2 on the mechanical properties of reservoir and cap rock. Energy Proc. 4, 5392–5397.

Park, J., Griffiths, L., Dautriat, J., Grande, L., Rodriguez, I., Iranpour, K., Bjørnarå, Marín-Moreno, H., Mondol, N., Sauvin, G., Sarout, J., Soldal, M., Oye, V., Dewhurst, D., Choi, J.C., Best, A., 2021. Induced-seismicity geomechanics for controlled CO2 storage in the North Sea. International Journal of Greenhouse Gas Control 115, 103614.

Pourmalek, A., Newell, A.J., Shariatipour, S.M., Butcher, A.S., Milodowski, A.E., Bagheri, M., Wood, A.M., 2021. Deformation bands in high-porosity sandstones: Do they help or hinder CO2 migration and storage in geological formations? International Journal of Greenhouse Gas Control 107, 103292.

Rigby, S.P., Alsayah, A., Seely, R., 2022. Impact of Exposure to Supercritical Carbon Dioxide on Reservoir Caprocks and Inter-Layers during Sequestration. Energies 15, 7538.

Rohmer, J., Seyedi, D.M., 2010. Coupled large scale hydromechanical modelling for caprock failure risk assessment of CO_2 storage in deep saline aquifers. Oil & Gas Science and Technology- Rev. IFP 65, 503–517.

Seyedi, D., Ducellier, A., Foerster, E., Guy, N., Hild, F., Rohmer, J., 2009. Coupled hydromechanical modeling to study the integrity and safety of geological storage of CO2. Energy Proc. 1, 2541–2548.

Shukla, R., Ranjith, P., Haque, A., Choi, X., 2010. A review of studies on CO2 sequestration and caprock integrity. Fuel 89, 2651–2664.

Springer, N., Lindgren, H., 2006. Caprock properties of the Nordland shale recovered from the 15/9-A11 well, the sleipner area. In: Reenhouse Gas Technology Conference 2006 (GHGT-8) Proceedings. Online]. Available: https://www.researchgate.net/publication/284510608_Caprock_properties_of_the_Nordland_Shale_recovered_from_the_159-A11_well_the_Sleipner_area. Accessed 1 NOV 2020.

Sundal, A., Miri, R., Aagaard, P., 2015. Modelling CO2 migration in aquifers; considering 3D seismic property data and the effect of site-typical depositional heterogeneities. Int. J. Greenh. Gas Control 39, 349–365.

Tran, D., Nghiem, L., Buchanan, L., 2005. An overview of iterative coupling between geomechanical deformation and reservoir flow. In: SPE/PS-CIM/CHOA International Thermal Operations and Heavy Oil Symposium Proceedings, 2005.

Tran, D., Shrivastava, V., Nghiem, L., Kohse, B., 2009. Geomechanical risk mitigation for CO2 sequestration in saline aquifers. In: SPE Annual Technical Conference and Exhibition. SPE-125167-MS.

Varre, S.B.K., Siriwardane, H.J., Gondle, R.K., Bromhal, G.S., Chandrasekar, V., Sames, N., 2015. Influence of geochemical processes on the geomechanical response of the overburden due to CO_2 storage in saline aquifers. Int. J. Greenh. Gas Control 42, 138–156.

Vidal-Gilbert, S., Nauroy, J.-F., Brosse, E., 2009. 3D geomechanical modelling for CO2 geologic storage in the Dogger carbonates of the Paris Basin. Int. J. Greenh. Gas Control 3, 288–299.

Williams, G., Chadwick, R., Vosper, H., 2018. Some thoughts on Darcy-type flow simulation for modelling underground CO 2 storage, based on the Sleipner CO 2 storage operation. Int. J. Greenh. Gas Control 68, 164–175.

Xiao, T.X.U.H., Moodie, N., Esser, R., Jia, W., Zheng, L., Rutqvist, J., Mcpherson, B., 2020. Chemical-mechanical impacts of CO_2 intrusion into heterogeneous caprock. Water Resour. Res. 56, e2020WR027193.

Yang, Y., Aplin, A., 2004. Definition and practical application of mudstone porosity-effective stress relationships. Petroleum Geoscience - PETROL GEOSCI 10, 153–162.

Zhang, G., Lu, P., Wei, X., Zhu, C., 2016. Impacts of mineral reaction kinetics and regional groundwater flow on long-term CO2 fate at sleipner. Energy Fuels 30, 4159–4180.

Zhou, X., Burbey, T.J., 2016. Numerical modeling of percolating flow path in a caprock formation during aquifer pressurization and its implication for CO_2 sequestration. Environ. Earth Sci. 75, 861.

Zweigel, P., Lothe, A.E., Arts, R., Hamborg, M.. Reservoir geology of the storage units in the Sleipner CO2-injection case- A contribution to the saline aquifer CO2 storage (SACS) project. Sintef Petroleum Research. https://www.sintef.no/globalassets/project/ik23430000-sacs/technical-reports/zweigeletal_2000_reservoirreport_text.pdf.

Nghiem, L., Sammon, P., Grabenstetter, J., Ohkuma, H., 2004. Modeling CO2 storage in aquifers with a fully-coupled geochemical EOS compositional simulator. SPE89474.

IEA, 2010. World Energy Report. https://www.iea.org/reports/world-energy-outlook-2010.